NAVAL POSTGRADUATE SCHOOL

MONTEREY, CALIFORNIA

THESIS

REDUCING STATOR CURRENT HARMONICS FOR A DOUBLY-FED INDUCTION GENERATOR CONNECTED TO A DISTORTED GRID

by

Seth J. Pierce

September 2013

Thesis Advisor: Alexander L. Julian
Second Reader: Roberto Cristi

THIS PAGE INTENTIONALLY LEFT BLANK

REPORT DOCUMENTATION PAGE		Form Approved OMB No. 0704-0188

1. AGENCY USE ONLY *(Leave blank)*	2. REPORT DATE September 2013	3. REPORT TYPE AND DATES COVERED Master's Thesis

4. TITLE AND SUBTITLE REDUCING STATOR CURRENT HARMONICS FOR A DOUBLY-FED INDUCTION GENERATOR CONNECTED TO A DISTORTED GRID	5. FUNDING NUMBERS
6. AUTHOR(S) Seth J. Pierce	
7. PERFORMING ORGANIZATION NAME(S) AND ADDRESS(ES) Naval Postgraduate School Monterey, CA 93943-5000	**8. PERFORMING ORGANIZATION REPORT NUMBER**
9. SPONSORING /MONITORING AGENCY NAME(S) AND ADDRESS(ES) N/A	**10. SPONSORING/MONITORING AGENCY REPORT NUMBER**

11. SUPPLEMENTARY NOTES The views expressed in this thesis are those of the author and do not reflect the official policy or position of the Department of Defense or the U.S. government. IRB protocol number ____N/A____.

12a. DISTRIBUTION / AVAILABILITY STATEMENT Approved for public release; distribution is unlimited	12b. DISTRIBUTION CODE A

13. ABSTRACT (maximum 200 words)

The Department of Defense (DoD) is increasing its demand for reliable renewable energy sources. The doubly-fed induction generator (DFIG) is widely used to extract electrical energy from wind and is a useful means for the DoD to achieve its renewable energy goals.

The DFIG is susceptible to electric grid voltage harmonics, which is a potential obstacle for implementing stable wind-energy systems. Two existing rotor voltage controllers are modeled in this thesis for eventual implementation in a laboratory DFIG wind energy system. The first controller uses multiple proportional-integral (PI) controllers to filter out the fifth and seventh stator current harmonics. Each PI controller operates in a reference frame that rotates in synchronicity with the harmonic that is being filtered. The second controller operates in the synchronous reference frame and simultaneously filters both the fifth and seventh stator current harmonics using a double integrator called a proportional-resonant controller (PR).

The PI controller is shown to be more effective at eliminating the stator current than the PR controller but has a slower reaction time. The PR controller requires fewer computations but has more stability concerns. Both controllers reduce torque oscillations resulting from the grid distortion by approximately the same amount.

14. SUBJECT TERMS doubly-fed induction generator, harmonic distortion, resonant controller	15. NUMBER OF PAGES 73
	16. PRICE CODE

17. SECURITY CLASSIFICATION OF REPORT	18. SECURITY CLASSIFICATION OF THIS PAGE	19. SECURITY CLASSIFICATION OF ABSTRACT	20. LIMITATION OF ABSTRACT
Unclassified	Unclassified	Unclassified	UU

NSN 7540-01-280-5500

Standard Form 298 (Rev. 2-89)
Prescribed by ANSI Std. 239-18

THIS PAGE INTENTIONALLY LEFT BLANK

Approved for public release; distribution is unlimited

REDUCING STATOR CURRENT HARMONICS FOR A DOUBLY-FED INDUCTION GENERATOR CONNECTED TO A DISTORTED GRID

Seth J. Pierce
Lieutenant, United States Navy
B.S. University of New Mexico, 2004

Submitted in partial fulfillment of the
requirements for the degree of

MASTER OF SCIENCE IN ELECTRICAL ENGINEERING

from the

NAVAL POSTGRADUATE SCHOOL
September 2013

Author: Seth J. Pierce

Approved by: Alexander L. Julian
Thesis Advisor

Roberto Cristi
Second Reader

R. Clark Robertson
Chair, Department of Electrical and Computer Engineering

THIS PAGE INTENTIONALLY LEFT BLANK

ABSTRACT

The Department of Defense (DoD) is increasing its demand for reliable renewable energy sources. The doubly-fed induction generator (DFIG) is widely used to extract electrical energy from wind and is a useful means for the DoD to achieve its renewable energy goals.

The DFIG is susceptible to electric grid voltage harmonics, which is a potential obstacle for implementing stable wind-energy systems. Two existing rotor voltage controllers are modeled in this thesis for eventual implementation in a laboratory DFIG wind energy system. The first controller uses multiple proportional-integral (PI) controllers to filter out the fifth and seventh stator current harmonics. Each PI controller operates in a reference frame that rotates in synchronicity with the harmonic that is being filtered. The second controller operates in the synchronous reference frame and simultaneously filters both the fifth and seventh stator current harmonics using a double integrator called a proportional-resonant controller (PR).

The PI controller is shown to be more effective at eliminating the stator current than the PR controller but has a slower reaction time. The PR controller requires fewer computations but has more stability concerns. Both controllers reduce torque oscillations resulting from the grid distortion by approximately the same amount.

THIS PAGE INTENTIONALLY LEFT BLANK

TABLE OF CONTENTS

LIST OF FIGURES

THIS PAGE INTENTIONALLY LEFT BLANK

LIST OF TABLES

THIS PAGE INTENTIONALLY LEFT BLANK

LIST OF ACRONYMS AND ABBREVIATIONS

AC	Alternating Current
DC	Direct Current
DFIG	Doubly-Fed Induction Generator
DFT	Discrete Fourier Transform
MRF	Multi-Rotating-Frame
NPS	Naval Postgraduate School
PI	Proportional Integral
PLL	Phase-Locked Loop
PR	Proportional Resonant

THIS PAGE INTENTIONALLY LEFT BLANK

EXECUTIVE SUMMARY

The Department of Defense (DoD) has a mandate to increase the energy its installations consume from renewable sources. The goal is for DoD installations to consume at least twenty-five percent of their electrical power from renewable sources by 2025 [1]. Wind energy is one of the areas that the Navy has identified as a maturing technology. The doubly-fed induction generator (DFIG) using a Scherbuis drive with a vector control strategy is a widely used means of extracting electrical energy from wind [2]. This DFIG configuration is susceptible to electric grid voltage distortion [3] [4] which could lead to problems in implementing it for DoD use. The goal of this thesis is to develop and examine models for two different rotor controllers [3] [4].

The operating speed of the DFIG can be adjusted to optimize turbine efficiency for given wind conditions. A common method for controlling the operating speed is to use a Scherbius drive with vector control as discussed in [2]. The Scherbius drive uses an AC–AC converter to excite the rotor. Vector control refers to the control strategy that decouples the magnetic flux and torque for ease of machine control. The Scherbius scheme using vector control does not eliminate stator current harmonics caused by distorted grid voltage. These harmonics lead to shaft torque oscillations, increased copper losses, and the possibility of exceeding harmonic current injection limits.

Several control methods have been published to reduce the stator current harmonics generated by the DFIG. A proportional resonant (PR) controller [3] and a multi-rotating-frame (MRF) control strategy [4] are examined in this thesis.

A DFIG wind energy conversion system (WECS) was established at the Naval Postgraduate School (NPS) by [5] and [6]. A block diagram for the WECS is shown in Figure 1.

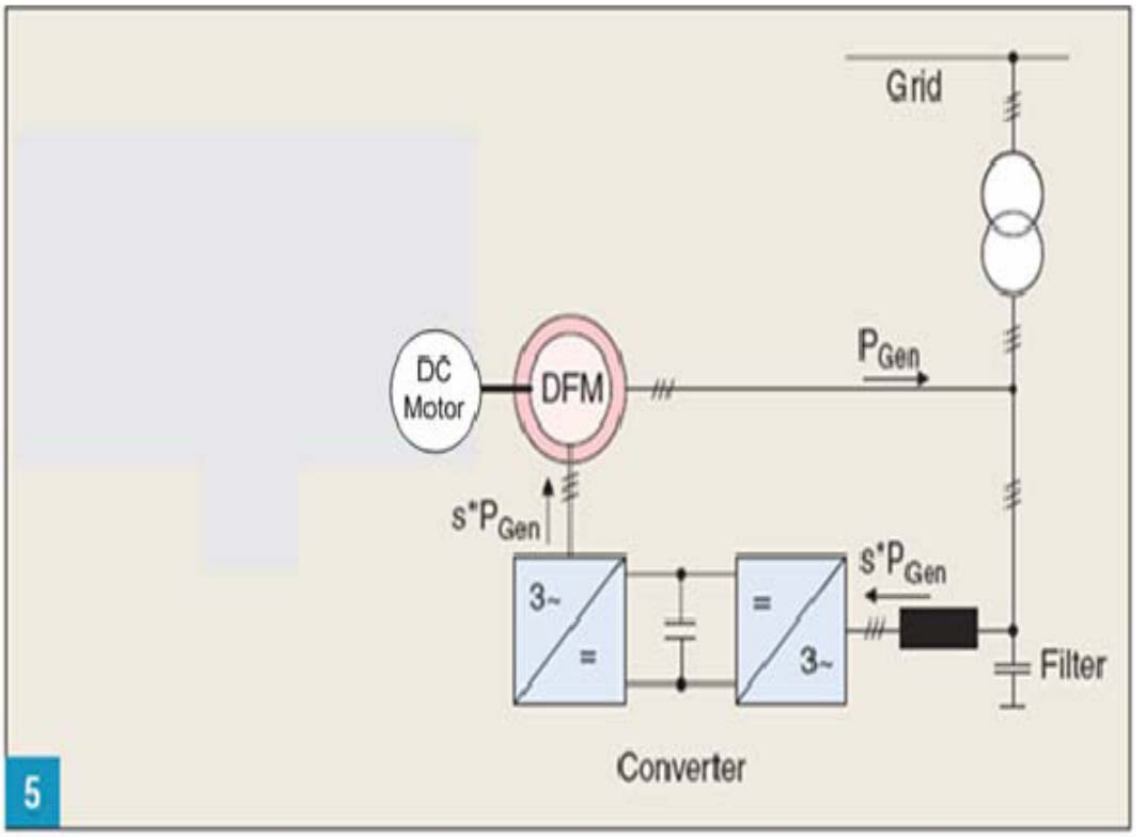

Figure 1. NPS WECS using a DC motor to simulate wind turbine input torque (From [6]).

The grid voltage present at the stator of the DFIG was measured, and the harmonic content was calculated. The voltage data was recorded for twelve consecutive cycles for both a super-synchronous and sub-synchronous data run. A plot of the phase B-to-phase C line voltage for the super-synchronous data run is shown in Figure 2.

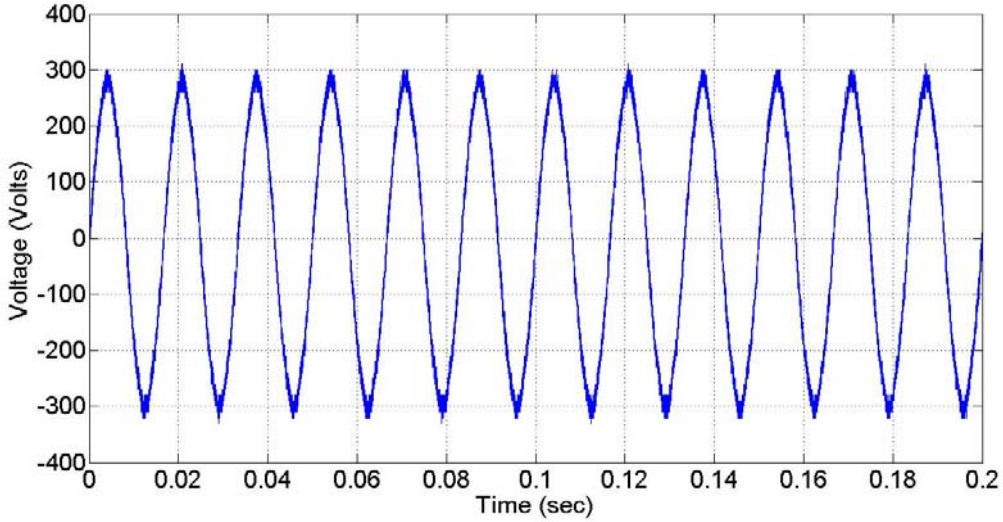

Figure 2. B-C line voltage for the super-synchronous data run.

The sub-synchronous B-C line voltage data is plotted and shown in Figure 3.

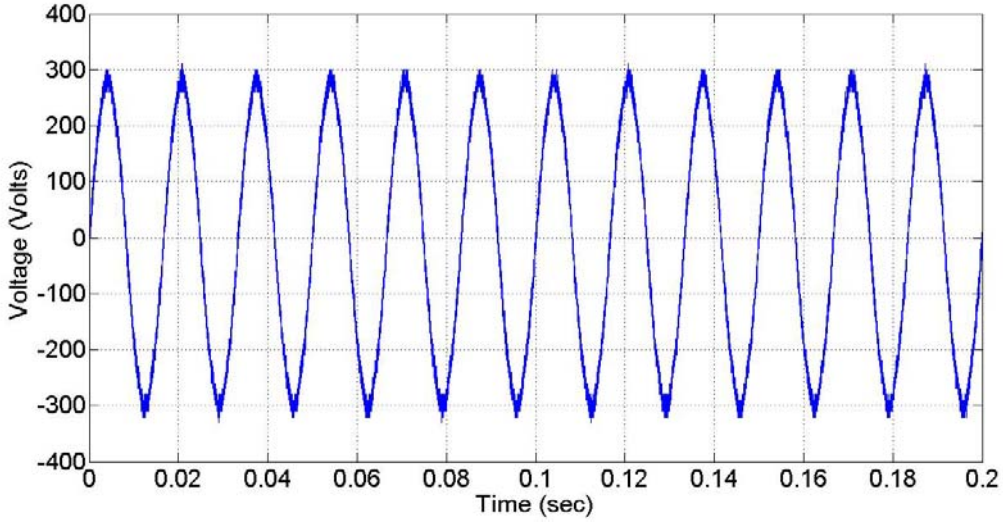

Figure 3. B-C line voltage for the sub-synchronous data run.

The harmonic content of the input voltage was calculated and is shown in Table 1.

Table 1. Fifth and seventh harmonic content of the grid voltage.

Harmonic	Sub-Synchronous Data Run (% of fundamental)	Super-Synchronous Data Run (% of fundamental)
Fifth	1.61%	1.45%
Seventh	0.61%	0.60%

The harmonic content of the stator current was also measured and compared to a previously developed DFIG WECS Simulink model [7]. The input voltage to the model had the same fifth and seventh harmonic distortion seen in the lab. The resulting stator current distortion in the model and the DFIG WECS are shown in Table 2.

Table 2. Actual versus simulated stator current harmonic content.

	Sub-Synchronous Operation		Super-Synchronous Operation	
	Actual	Simulated	Actual	Simulated
Fifth Harmonic Stator Current (% of fundamental)	1.85	1.90	1.65	1.95
Seventh Harmonic Stator Current (% of fundamental)	0.73	0.83	0.63	0.67

Rotor controllers based on the PR method [3] and MRF method [4] were developed and applied to the Simulink model. The reduction in stator current harmonics from the MRF controller is shown in Table 3.

Table 3. Stator current harmonic content before and after MRF controller activation.

	Sub-Synchronous Operation		Super-Synchronous Operation	
	Before Activation	After Activation	Before Activation	After Activation
Fifth Harmonic Stator Current (% of fundamental)	1.90	5.62×10^{-5}	1.95	7.02×10^{-5}
Seventh Harmonic Stator Current (% of fundamental)	0.83	1.75×10^{-5}	0.67	1.84×10^{-5}

The effect of MRF controller on electromagnetic torque pulsations for the sub-synchronous data run is shown in Figure 4.

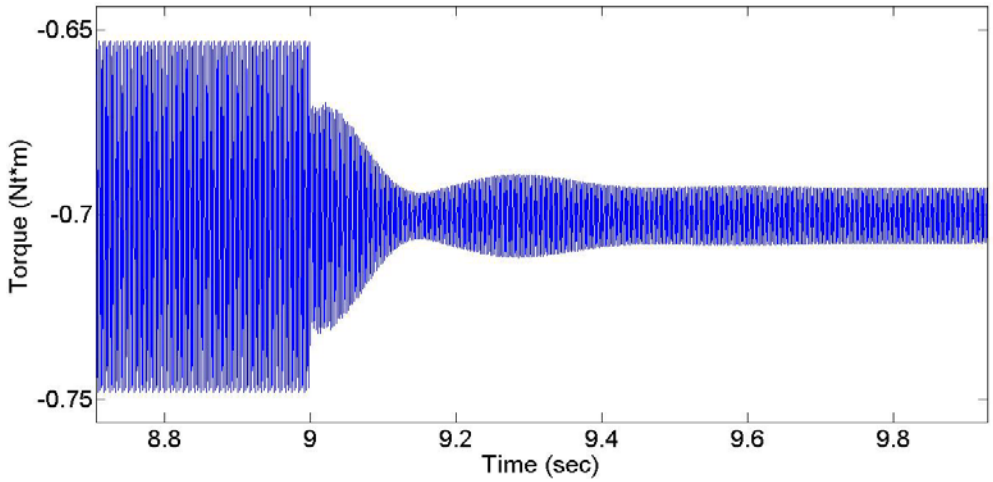

Figure 4. Effect of MRF controller on electromagnetic torque for the sub-synchronous data run.

The MRF and PR controllers were activated at nine seconds in all data runs. The effect of MRF controller on electromagnetic torque pulsations for the super-synchronous data run is shown in Figure 5.

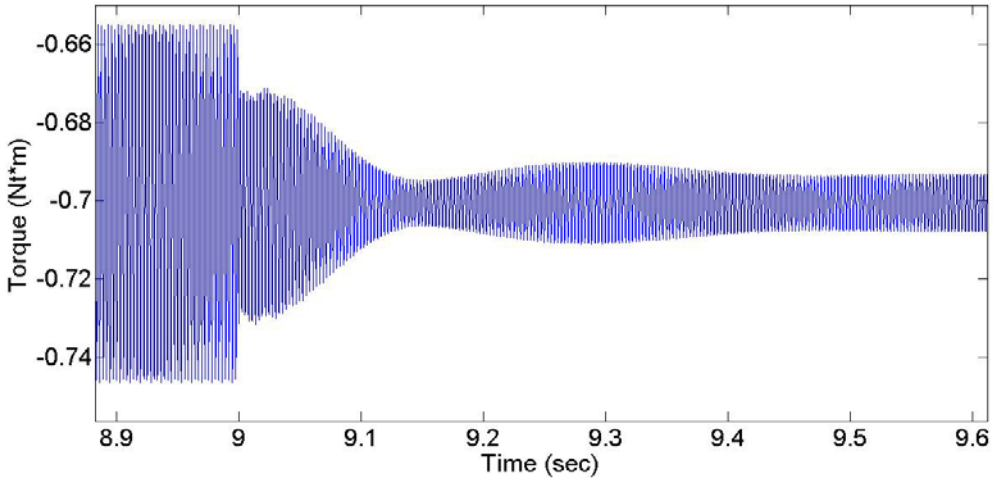

Figure 5. Effect of MRF controller on electromagnetic torque for the super-synchronous data run.

The reduction in stator current harmonic content is shown in Table 4. The controller was tested with a resonant gain $K_r = 1000$ and $K_r = 10000$ to illustrate the steady-state error's dependence on K_r. The results match the assertion made in [3] that the steady-state error varies approximately as the inverse of K_r. The reduction in the electrical torque fluctuation for the sub-synchronous data run is shown in Figure 5.

Table 4. Stator current harmonic content before and after PR controller activation.

	Sub-Synchronous Operation			Super-Synchronous Operation		
	Before Activation	After Activation		Before Activation	After Activation	
		K_r=1000	K_r=10000		K_r=1000	K_r=10000
5th Harmonic Current (% of fundamental)	1.90	0.32	0.063	1.95	0.34	0.064
7th Harmonic Current (% of fundamental)	0.83	0.14	0.031	0.67	0.12	0.026

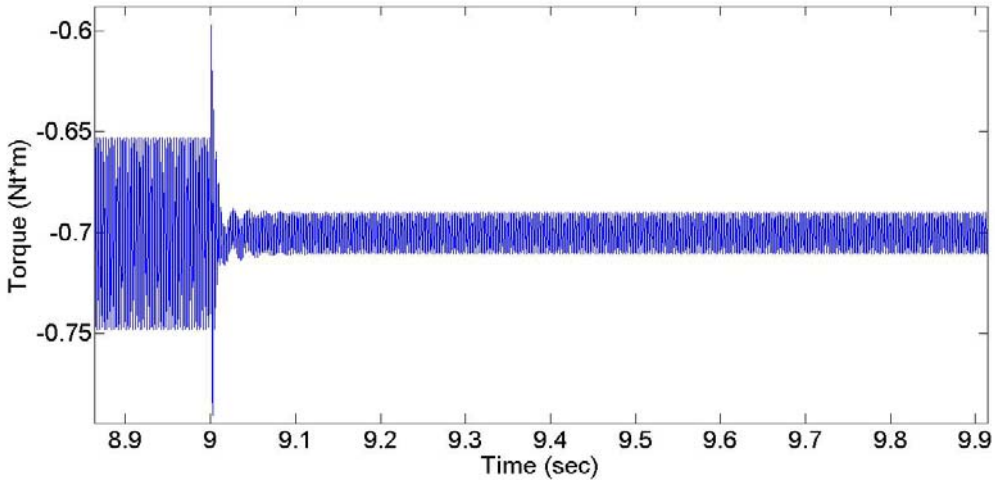

Figure 5. Effect of PR controller on electromagnetic torque for the sub-synchronous data run.

The reduction in the electrical torque fluctuation for the super-synchronous data run is shown in Figure 6.

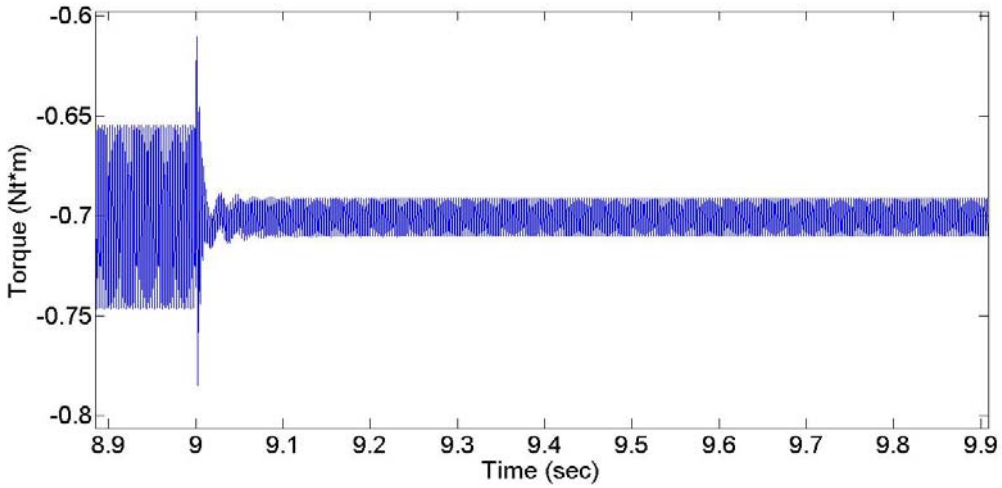

Figure 6. Effect of PR controller on electromagnetic torque for the super-synchronous data run.

The PR controller was enabled at nine seconds for both data runs and the torque fluctuations for both $K_r = 1000$ and $K_r = 10000$ were reduced to approximately twenty percent of their original value.

Both PR and MRF controllers would be viable options for reducing the harmonic content of the stator current for the DFIG. The advantages and disadvantages for each type of controller are summarized in Table 5.

Table 5. Advantages and disadvantages for the MRF and PR controllers.

Controller Type	**Advantages**	**Disadvantages**
PR	1. Fast response (<0.1 seconds to reach steady state once enabled) 2. Reduced torque fluctuations by 80% 3. Simultaneously filters both the fifth and seventh harmonics	1. Less reduction in stator current harmonics
MRF	1. Reduced torque fluctuations by 80% 2. Significantly reduced stator current harmonics	1. Slower response (approximately 0.5 seconds to reach steady state once enabled) 2. A controller is required for each harmonic

Both controllers reduced the harmonic content of the stator current and the torque fluctuations. The stator current harmonic reduction for each controller was adequate to reduce the torque fluctuations to approximately the minimum value possible. The remaining torque fluctuations were caused by the fluctuation in the stator flux, which was the result of the grid voltage harmonics. A stable DFIG wind system would be a great way to help the Department of Defense reach the goal of 25 percent renewable energy by 2025.

LIST OF REFERENCES

[1] John Warner National Defense Authorization Act for Fiscal Year 2007, Public Law no. 109-364, section 2852, 2006.

[2] R. Pena et al., "Doubly fed induction generator using back-to-back PWM converters and its application to variable-speed wind-energy generation," *IEEE Proc. Electr. Power Appl.*, vol. 143, no. 3, pp. 231–241, May 1996.

[3] L. Changjin et al., "Stator current harmonic control with resonant controller for doubly fed induction generator," *IEEE Trans. on Power Electronics*, vol. 27, no.7, pp. 3207–3220, July 2012.

[4] C. Wenjie, X Jun, Z Nan, L Changjin, C Min, X Dehong, "Stator harmonic current suppression for DFIG wind power system under distorted grid voltage," *3rd IEEE International Symposium on Power Electronics for Distributed Generation Systems*, Aalborg, Denmark, pp. 307–314, 2012.

[5] G. W. Edwards, "Wind Power Generation Emulation via Doubly-Fed Induction Generator Control," master's thesis, Naval Postgraduate School, Monterey, CA 2009.

[6] J. R. Derges, "Torque control of a separate-winding excitation DC motor for a dynamometer," master's thesis, Naval Postgraduate School, Monterey, CA 2010.

[7] A. L. Julian, "Induction machine model operating as an asynchronous generator," class notes for EC4130 (Advanced Electrical machinery Systems), Naval Postgraduate School, Monterey, CA, summer 2012.

THIS PAGE INTENTIONALLY LEFT BLANK

ACKNOWLEDGMENTS

I would like to thank my beautiful and amazing wife, Stephany, for all of the love and support during my research. I would also like to thank my three children, Seth, William, and Alyson, for being my inspiration and always bringing a smile to my face. I love you all very much.

I would also like to thank Dr. Alexander Julian for guiding me through this process and providing invaluable insight that helped make this thesis a great experience.

THIS PAGE INTENTIONALLY LEFT BLANK

I. INTRODUCTION

A. BACKGROUND

The National Defense Authorization Act for Fiscal Year 2007 established an official goal that 25 percent of the energy consumed by Department of Defense facilities must be from renewable sources by 2025 [1]. The United States Navy has identified wind energy as a maturing renewable energy technology. Wind energy will be a key enabler in reaching the 25 percent renewable consumption goal.

The doubly-fed induction generator (DFIG) is one of the options used to extract energy from wind. The DFIG can produce power at varying speeds, and most of the power produced bypasses the power electronics used for system control. These characteristics have allowed the DFIG to be the generator of choice for wind power systems.

The operating speed of the DFIG can be adjusted to optimize turbine efficiency for given wind conditions. A common method for controlling the operating speed is to use a Scherbius drive with vector control as discussed in [2]. The Scherbius drive uses an AC–AC converter to excite the rotor. Vector control refers to the control strategy that decouples the magnetic flux and torque for ease of machine control. However, the Scherbius scheme using vector control does not eliminate stator current harmonics caused by distorted grid voltage. These harmonics lead to shaft torque oscillations, increased copper losses, and the possibility of exceeding harmonic current injection limits.

Several control methods have been published to reduce the stator current harmonics generated by the DFIG. A proportional resonant (PR) controller [3] and a multi-rotating-frame (MRF) control strategy [4] are examined in this thesis.

B. OBJECTIVE

The goal of this thesis is to produce a computer model of a harmonic reduction controller for the DFIG used at the Naval Postgraduate School (NPS) Electrical

Machinery Laboratory from [5] and [6]. A resonant control harmonic reduction strategy and a multi-rotating-frame control harmonic reduction strategy are analyzed and compared in this thesis.

C. APPROACH

The approach of this thesis involved developing a computer model for the PR and the MRF control topologies. A computer model of the DFIG with the Scherbius scheme was compared to the laboratory measurements to build confidence that the simulation accurately predicts the current harmonic distortion that is present in the hardware. This was done by taking several measurements on the DFIG system in the laboratory as described in [5] and [6]. A basic diagram of the DFIG system used at NPS is shown in Figure 1.

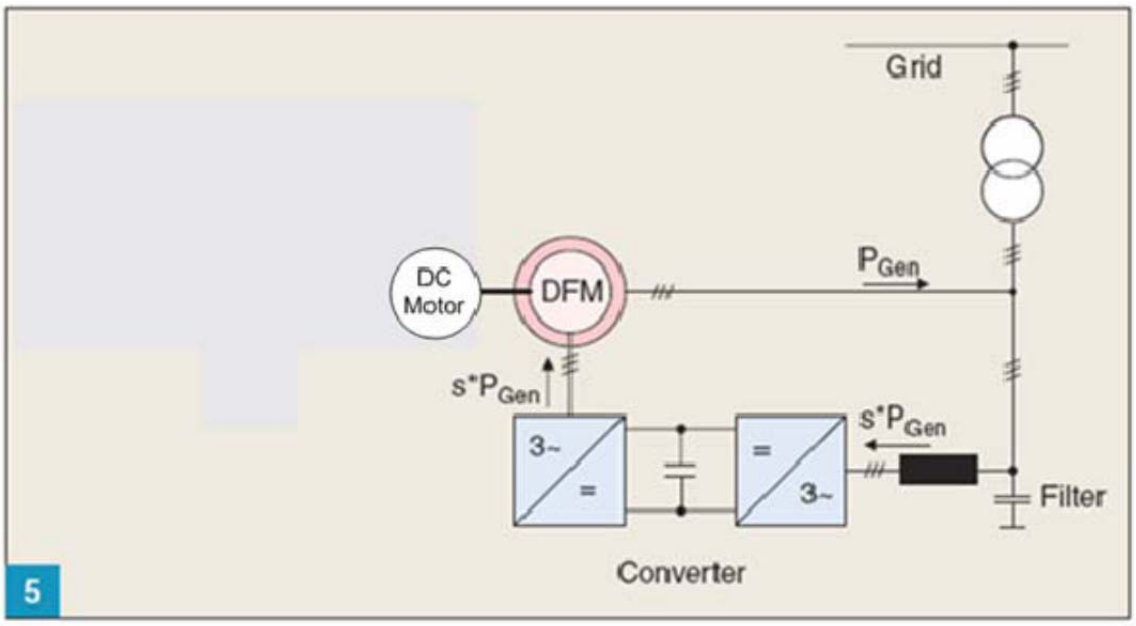

Figure 1. DFIG system used at NPS (From [6]).

The stator voltage and current were recorded during sub-synchronous and super-synchronous operating conditions. The stator voltage was then analyzed for harmonic content. The measured source voltage conditions were then applied to a Simulink model

of the DFIG system. The harmonic currents generated in the model were verified to be consistent with the measured data.

After the DFIG model's harmonic behavior was verified, the PR and MRF controller models were developed in the simulation. The controllers were then simulated under a variety of conditions for tuning and performance testing. The results of those simulations were then analyzed to obtain a better understanding of each control technique.

D. THESIS ORGANIZATION

This thesis consists of five chapters and an appendix. A brief description of why voltage harmonics are present on the grid and why they are undesirable is given in Chapter II.

The operation of the DFIG system used to extract wind energy is covered in Chapter III. The basic theory behind DFIG operation is discussed, followed by an explanation of the vector control strategy used on the rotor of the DFIG. The Simulink model of the DFIG is also explained.

An examination of the PR and MRF controller topologies is contained in Chapter IV. The theory behind each controller is followed by the explanation of the Simulink models used to implement stator current harmonic rejection. The data obtained from simulating each controller is presented in this chapter.

The conclusions drawn from testing the PR and MRF controllers is presented in Chapter V. Future research suggestions are also made in this final chapter of the thesis.

The Appendix contains all of the Matlab code and Simulink model diagrams applicable to this thesis.

THIS PAGE INTENTIONALLY LEFT BLANK

II. ELECTRIC GRID HARMONICS

A fundamental understanding of grid voltage harmonics is vital in developing a controller to reduce their negative effects. The concepts necessary to develop a controller that can be used to filter low order current harmonics that are present in the stator of the DIFG because of the voltage distortion in the AC bus (specifically the negative sequence fifth and positive sequence seventh harmonics) are explained in this chapter.

A. INTRODUCTION TO HARMONICS

Voltage harmonics are present on the electrical grid because of the use of non-linear electrical loads. Static power converters and overloaded transformers are two examples of non-linear loads that contribute to harmonic distortion on the grid. The DFIG is also, to a lesser extent, a contributor of harmonic current to the grid. Standards exist, such as the IEEE 519 [7], to control the harmonic quality of the voltage sources and the load currents present on the electrical grid. Despite these standards, grid voltage distortion still exists. Even harmonics are not considered in this thesis due to the half-wave symmetry of most non-linear loads, which results in the absence of even harmonics in the grid voltage. Odd triplen harmonics (such as the third and ninth) are not considered here due to their relatively low presence on the grid. The fifth and seventh voltage harmonics are examined in this thesis due to their relative abundance on the grid and their negative effects on both the grid and the DFIG.

1. Negative Sequence Fifth and Positive Sequence Seventh Voltage Harmonics

An important aspect of both the PR and MRF control strategies is the phasor rotation of the fifth and seventh voltage harmonics. For simplicity, consider the operation of a three-phase AC machine with two poles per phase. When a three-phase, 60 Hz voltage signal is applied, the sum of the three-phase voltages results in a voltage phasor rotating at 3600 rpm. This is considered the fundamental voltage phasor. If the individual phase voltages contained the fifth and seventh harmonics, the overall voltage phasor would be distorted. It follows that the phasor associated with the fifth harmonic

would rotate at 18,000 rpm and the seventh at 25,200 rpm. The relative directions of rotation are not necessarily obvious. The time delay between phase A and B of the fundamental voltage signal is one-third of the fundamental period. This time delay affects the fifth and seventh harmonic in opposite ways. Assuming a positive sequence fundamental rotation (ABC), the fifth harmonic in the B phase has a $5(4\pi/3) = 20\pi/3$ initial phase. This is equivalent to $2\pi/3$, while the initial phase angle for phase C is shifted to $4\pi/3$. This phase shift results in the fifth harmonic rotation in the negative sequence direction (ACB). The seventh harmonic's B phase is shifted by $7(4\pi/3) = 28\pi/3$, which is equivalent to $4\pi/3$. This phase angle is the same as the fundamental phase angle for phase B. An equivalent argument can be made for phase C, which results in an overall seventh harmonic voltage phasor that rotates in the same direction as the fundamental (ABC).

The negative sequence fifth and positive sequence seventh harmonic rotation direction is a key point to understand when executing the reference frame shifts that occur in both the PR and MRF control s topologies.

2. Adverse Impact of Voltage and Current Harmonics

The adverse effects of electrical harmonics are discussed in great detail in [7]. The presence of voltage harmonics on the grid make the DFIG susceptible to increased copper and iron losses, increased audible noise emission due to induced vibrations, and mechanical stress due to torque pulsations. Additionally, the DFIG using the Scherbius control scheme has the potential to pass these voltage harmonics through to the stator current, possibly amplified [3]. Under certain conditions, these current harmonics could cause the DFIG to be in violation of grid harmonic standards such as [7].

B. MEASURED GRID VOLTAGE HARMONICS

The grid voltage distortion present at the NPS Electrical Machinery Lab was measured in order to verify the accuracy of the DFIG computer model used in this thesis. Two sets of data were taken, each 0.2 seconds in duration. The data sets consist of the phase A stator line current I_{AS} and the line voltage measured from phase B to phase C of

the DFIG V_{BC}. One data set corresponds to a sub-synchronous DFIG condition, while the other set corresponds to a super-synchronous condition. These DFIG operating conditions are explained in more detail in Chapter III. The harmonic content of V_{BC} is relevant to this chapter and is independent of the DFIG operating conditions. It is important to accurately measure the grid voltage harmonics to ensure that the simulated DFIG receives the appropriate input voltage signal. The computer model of the DFIG can then be evaluated by comparing the simulated versus measured output current.

1. Grid Voltage Measurement

The measured voltage was obtained by using an oscilloscope with a sampling frequency of 500 kHz and duration of 0.2 seconds. The data was then imported into Matlab and analyzed. The input line voltage V_{BC} for the super-synchronous data run is shown below in Figure 2.

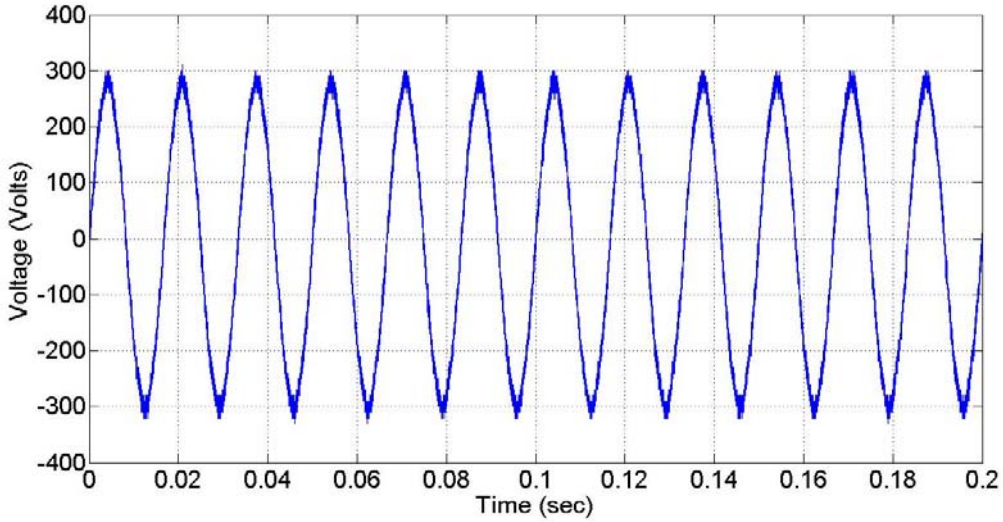

Figure 2. B-C line voltage for the super-synchronous data run.

The input line voltage V_{BC} for the sub-synchronous data run is shown in Figure 3.

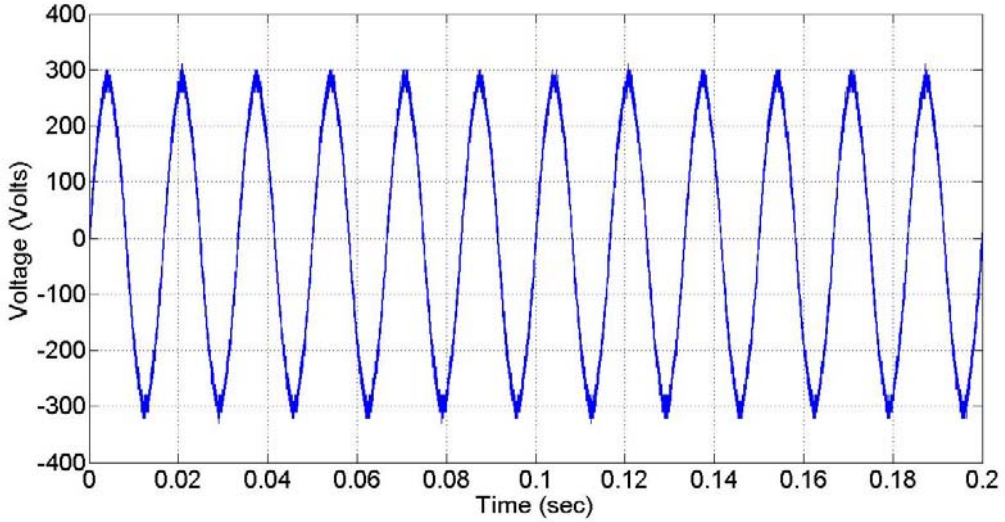

Figure 3. B-C line voltage for sub-synchronous data run.

2. Calculation of Grid Voltage Harmonic Content

The harmonic components of the grid voltage were determined by using a discrete Fourier transform (DFT). The DFT coefficients were used to reconstruct the grid voltage as a Fourier series. The theory behind these calculations was taken from [8].

A DFT is performed over each of the 12 cycles of the input V_{BC} shown in Figures 2 and 3. The DFT of a single period of V_{BC} is given by

$$a_k = \frac{1}{N}\sum_{n=0}^{N-1} x_n e^{-i2\pi kn/N} \tag{1}$$

where a_k is the DFT coefficient, x_n is the sampled voltage signal V_{BC}, N is the number of samples in one period of the waveform, and k is the integer multiple of the fundamental frequency for the harmonic coefficient that is being calculated. The original signal can be reconstructed as a Fourier series using the a_k coefficients from

$$V_{BC}(t) = a_0 + 2\sum_{k=1}^{N-1}\left|a_k\right|\cos\left(2\pi k f_o t + \tan^{-1}\left(\frac{\mathrm{Im}(a_k)}{\mathrm{Re}(a_k)}\right)\right) \tag{2}$$

where f_o is the fundamental frequency (60 Hz), and t is time.

The DFT coefficients for each of the 12 cycles of measured V_{BC} were averaged, and the results for the fifth and seventh harmonic are shown in Table 1.

Table 1. Grid voltage fifth and seventh harmonic content.

Harmonic	Sub-Synchronous Data Run (% of fundamental)	Super-Synchronous Data Run (% of fundamental)
Fifth	1.61%	1.45%
Seventh	0.61%	0.60%

The harmonic percentages are less than the three percent limit for individual harmonics listed in [7]. These harmonic percentages were the values injected into the DFIG computer model. The phase angles of the measured fifth and seventh harmonics in the lab were also passed to the simulation. A detailed discussion of the voltage harmonic effects on the DFIG is contained in Chapter IV.

C. CHAPTER SUMMARY

The background information on grid voltage harmonics necessary to understand the PR and MRF controllers was presented in this chapter. The negative effects of these harmonics on the DFIG were also explained. Finally, the method for measuring harmonics present at the NPS DFIG was explained.

THIS PAGE INTENTIONALLY LEFT BLANK

III. DFIG OPERATION

An understanding of the basic principles of operation of the vector controlled DFIG is crucial to realizing a solution to the problem of undesired stator current harmonics. The foundation of knowledge necessary to understand the operation of the PR and MRF controllers is provided in this chapter.

A DFIG is simply an induction machine with external rotor excitation. The external rotor excitation controls the magnetic field induced on the rotor and, therefore, can control aspects of the machine operation. The rotor excitation circuit, when working properly, induces a magnetic flux on the rotor that rotates in synchronicity with the stator flux. As the rotor speed changes due to external factors (i.e., wind speed), the rotor excitation circuit adjusts the frequency of the applied rotor voltage to maintain synchronous operation. The ability to provide power at varying rotor speed is one of the major advantages to using a DFIG in a wind energy conversion system.

A. DFIG MACHINE EQUATIONS

The equations used to model the DFIG were taken from [9]. The equations for the arbitrary reference frame rotor and stator current are given by

$$i_{qs} = \frac{1}{X_{ls}}\left(\psi_{qs} - \psi_{mq}\right), \tag{3}$$

$$i_{ds} = \frac{1}{X_{ls}}\left(\psi_{ds} - \psi_{mq}\right), \tag{4}$$

$$i_{0s} = \frac{1}{X_{ls}}\psi_{0s}, \tag{5}$$

$$i'_{qr} = \frac{1}{X'_{lr}}\left(\psi'_{qr} - \psi_{mq}\right), \tag{6}$$

$$i'_{dr} = \frac{1}{X'_{lr}}\left(\psi'_{dr} - \psi_{mq}\right), \tag{7}$$

and

$$i'_{0r} = \frac{1}{X'_{lr}}\psi'_{0r} \tag{8}$$

where the i is current, ψ is flux linkage per second, and X is reactance; the subscripts q, d, 0 are the $qd0$ reference frame components; the subscripts s and r are stator and rotor; and the subscript m stands for mutual. The equations for the mutual flux linkage per second terms are given by

$$\psi_{mq} = X_M \left(i_{qs} + i'_{qr} \right) \tag{9}$$

and

$$\psi_{md} = X_M \left(i_{ds} + i'_{dr} \right). \tag{10}$$

The flux linkage per second equations in terms of voltage are given by

$$\psi_{qs} = \frac{\omega_b}{p}\left[v_{qs} - \frac{\omega}{\omega_b}\psi_{ds} + \frac{r_s}{X_{ls}}\left(\psi_{mq} - \psi_{qs} \right) \right], \tag{11}$$

$$\psi_{ds} = \frac{\omega_b}{p}\left[v_{ds} - \frac{\omega}{\omega_b}\psi_{qs} + \frac{r_s}{X_{ls}}\left(\psi_{mq} - \psi_{ds} \right) \right], \tag{12}$$

$$\psi_{0s} = \frac{\omega_b}{p}\left[v_{0s} - \frac{r_s}{X_{ls}}\psi_{0s} \right], \tag{13}$$

$$\psi'_{qr} = \frac{\omega_b}{p}\left[v'_{qr} - \left(\frac{\omega - \omega_r}{\omega_b} \right)\psi'_{dr} + \frac{r'_r}{X'_{lr}}\left(\psi_{mq} - \psi'_{qr} \right) \right], \tag{14}$$

$$\psi'_{dr} = \frac{\omega_b}{p}\left[v'_{dr} - \left(\frac{\omega - \omega_r}{\omega_b} \right)\psi'_{qr} + \frac{r'_r}{X'_{lr}}\left(\psi_{mq} - \psi'_{dr} \right) \right], \tag{15}$$

$$\psi'_{0r} = \frac{\omega_b}{p}\left[v'_{0r} - \frac{r'_r}{X'_{lr}}\psi'_{0r} \right], \tag{16}$$

$$\psi_{mq} = X_{aq}\left(\frac{\psi_{qs}}{X_{ls}} + \frac{\psi'_{qr}}{X'_{lr}} \right), \tag{17}$$

and

$$\psi_{md} = X_{ad}\left(\frac{\psi_{ds}}{X_{ls}} + \frac{\psi'_{dr}}{X'_{lr}} \right) \tag{18}$$

where ω_b is the electrical angular velocity, ω is the reference frame velocity, ω_r is the rotor angular velocity, p is the operator d/dt and

$$X_{aq} = X_{ad} = \left(\frac{1}{X_M} + \frac{1}{X_{ls}} + \frac{1}{X'_{lr}} \right)^{-1}. \tag{19}$$

The equations for per unit electrical torque T_e and ω_r are given by

$$T_e = \left(\frac{3}{2}\right)\left(\frac{P}{2}\right)\left(\frac{1}{\omega_b}\right)\left(\psi_{ds} i_{qs} - \psi_{qs} i_{ds}\right) \tag{20}$$

and

$$\omega_r = \frac{1}{p}\left[\frac{P}{2J}\left(T_e - T_L\right)\right] \tag{21}$$

where T_L is the mechanical torque applied to the shaft, J is the inertia of the rotor, and P is the number of poles per phase.

Equations (11)–(18) are used in the Simulink model to calculate the flux linkage per second quantities of the DFIG. Rotor and stator current are determined by (3)–(8), while electrical torque and rotor angular speed are determined by (20) and (21), respectively. The uncontrolled DFIG model is made up of these equations. The next step is to apply the rotor control circuit. The operation of the rotor controller is explained in the next section.

B. VECTOR CONTROL OF DFIG

The vector control strategy is used in the NPS DFIG for its proven effectiveness and simplicity. Vector control decouples the control of electrical torque and rotor excitation [2]. This decoupling is achieved by aligning the *d*-axis of a synchronously rotating *qd*0 reference frame with the peak of the stator flux. This results in the elimination of the *q*-axis stator flux. The resulting torque equation now becomes [2]

$$T_e = -3\frac{P}{2} L_m i_{ms} i_{qr} \tag{22}$$

where L_m is the mutual inductance between the stator and rotor, and i_{ms} is the stator magnetizing current. This means that the T_e can be controlled directly by controlling i_{qr}. Controlling the T_e means that the speed can be controlled, and thus, for a given input torque T_L, output power can be controlled.

Reactive power flow control can be achieved by controlling i_{dr}, but this is typically achieved through a stator controller. The *d*-axis rotor current is commanded to be zero for this thesis.

C. COMPUTER SIMULATION OF VECTOR CONTROLLED DFIG

The vector controlled DFIG Simulink model used was based upon a previously developed model [10] of the NPS DFIG system. The operation of the model and the process used to validate the model are discussed in this section.

1. Rotor Controller

The Simulink model of the DFIG used in this thesis calculates the various machine parameters using (3)–(8), (11)–(18), (20), and (21). The reference frame used is one that rotates along with the rotor. In order to use the vector control strategy, the rotor controller needs to measure i_{qdr} (synchronous reference frame) and ω_r. The rotor controller senses i_{qdr} and ω_r and then commands v_{qdr} to achieve the desired results. The torque is controlled by v_{qr} which influences i_{qr}. Controlling the torque enables speed control. Since reactive power control is not desired in this thesis, i_{dr} is commanded to be zero by v_{dr}. A block diagram of the rotor control circuit is shown in Figure 4.

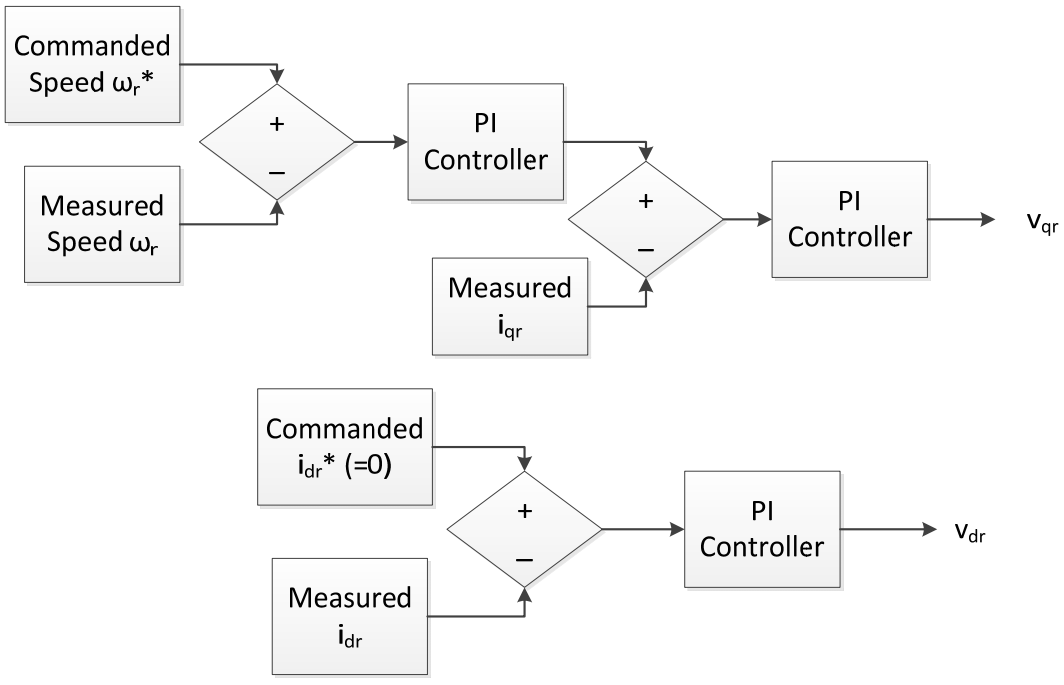

Figure 4. DFIG rotor controller diagram for vector control.

The proportional integral (PI) controller gains were chosen to ensure that the outer speed control loop was slower than the inner rotor current control loops. The gains chosen match the actual DFIG gains and are displayed in Table 2.

Table 2. Rotor controller PI gains.

	Speed Control Loop	Rotor Current Control Loop
Proportional Gain	0.066	75
Integral Gain	0.0132	40

2. Reference Frames

The machine parameters are developed in the rotor reference frame, while the machine equations are developed in the rotor reference frame. This difference in reference frames means that the variables have to be transformed from one frame to another. This transformation is accomplished with [9]

$$f_{qd0s}^{y} = {}^{x}K^{y} f_{qd0s}^{x} \tag{23}$$

where f_{qd0s}^{x} are the variables in the reference frame being transferred from, f_{qd0s}^{y} are the variables in the desired reference frame, and ${}^{x}K^{y}$ is the transformation matrix given by

$${}^{x}K^{y} = \begin{pmatrix} \cos(\theta_y - \theta_x) & -\sin(\theta_y - \theta_x) & 0 \\ \sin(\theta_y - \theta_x) & \cos(\theta_y - \theta_x) & 0 \\ 0 & 0 & 1 \end{pmatrix} \tag{24}$$

where θ is the angle of the *q*-axis of the arbitrary reference frame to the stationary reference frame. The superscripts e and r are used to denote the synchronous and rotor reference frames, respectively.

Park transformations are also used in the model to go from the stationary reference frame to the arbitrary *qd*0 reference frame. This transformation is done using

$$f_{qd0s} = K_s f_{abcs} \tag{25}$$

where f_{abcs} represents the stationary reference frame variables and K_s is the matrix [9]

$$K_s = \frac{2}{3}\begin{pmatrix} \cos\theta & \cos\left(\theta - \frac{2\pi}{3}\right) & \cos\left(\theta + \frac{2\pi}{3}\right) \\ \sin\theta & \sin\left(\theta - \frac{2\pi}{3}\right) & \sin\left(\theta + \frac{2\pi}{3}\right) \\ \frac{1}{2} & \frac{1}{2} & \frac{1}{2} \end{pmatrix}. \tag{26}$$

The inverse transformation is given by [9]

$$(K_s)^{-1} = \begin{pmatrix} \cos\theta & \sin\theta & 1 \\ \cos\left(\theta - \frac{2\pi}{3}\right) & \sin\left(\theta - \frac{2\pi}{3}\right) & 1 \\ \cos\left(\theta + \frac{2\pi}{3}\right) & \sin\left(\theta + \frac{2\pi}{3}\right) & 1 \end{pmatrix} \tag{27}$$

The calculation of the difference between the rotor reference frame angle θ_r and the synchronous reference frame *d*-axis flux angle is vital to achieving proper vector control of the DFIG. The angle θ_{slip} is calculated in the rotor reference frame using the *q* and *d*-axis stator voltages by

$$\theta_{slip} = \tan^{-1}\left(-\frac{v_{ds}^r}{v_{qs}^r}\right). \tag{28}$$

The θ_{slip} allows the rotor reference frame variables to be transformed into the synchronous reference frame using (23). The rotor controller then determines the appropriate v_{qr}^e and v_{dr}^e in the synchronous frame. These rotor voltages are then transformed back into the rotor reference frame and fed back into the machine equations.

3. DFIG Performance in the Presence of Grid Voltage Harmonics

The vector control method of the DFIG has shown degraded performance in the presence of grid voltage harmonics [3] [4]. Grid voltage harmonics tend to cause harmonics in both the DFIG's rotor and stator currents. These harmonics lead to the problems discussed in Chapter II. As previously discussed, the aim of this thesis is to minimize the harmonics generated in the stator current.

The validity of the DFIG model was determined prior to designing a harmonic rejection controller model. First, the actual DFIG stator current and voltage harmonics were measured during sub-synchronous and super-synchronous operations. The commanded speeds were 20 percent below and 10 percent above synchronous speed. The applied torque was held approximately constant for both data runs by applying 0.85 amperes to the DC motor that is used to simulate the torque input from the wind turbine. The data was taken as described in Chapter II.B. The harmonic content of the stator current and voltage was then determined using the previously described DFT method. Once the harmonic content of the supply voltage was calculated, the grid voltage was reconstructed in Simulink to test the response of the DFIG model. The reconstructed grid voltage consists of fundamental voltage, the fifth harmonic voltage, and the seventh harmonic voltage with the appropriate magnitude and phase. The Simulink model of the reconstructed three-phase grid voltage is shown in Figure 5.

The DFIG model was operated with the distorted source voltage and allowed to reach steady-state. Once steady-state was achieved, the harmonic content of I_{as} was calculated and compared with the measured stator current harmonic content of the DFIG. The results of this analysis are shown in Table 3.

Table 3. Actual versus simulated stator current harmonic content.

	Sub-Synchronous Operation		Super-Synchronous Operation	
	Actual	Simulated	Actual	Simulated
Fifth Harmonic Stator Current (% of fundamental)	1.85	1.90	1.65	1.95
Seventh Harmonic Stator Current (% of fundamental)	0.73	0.83	0.63	0.67

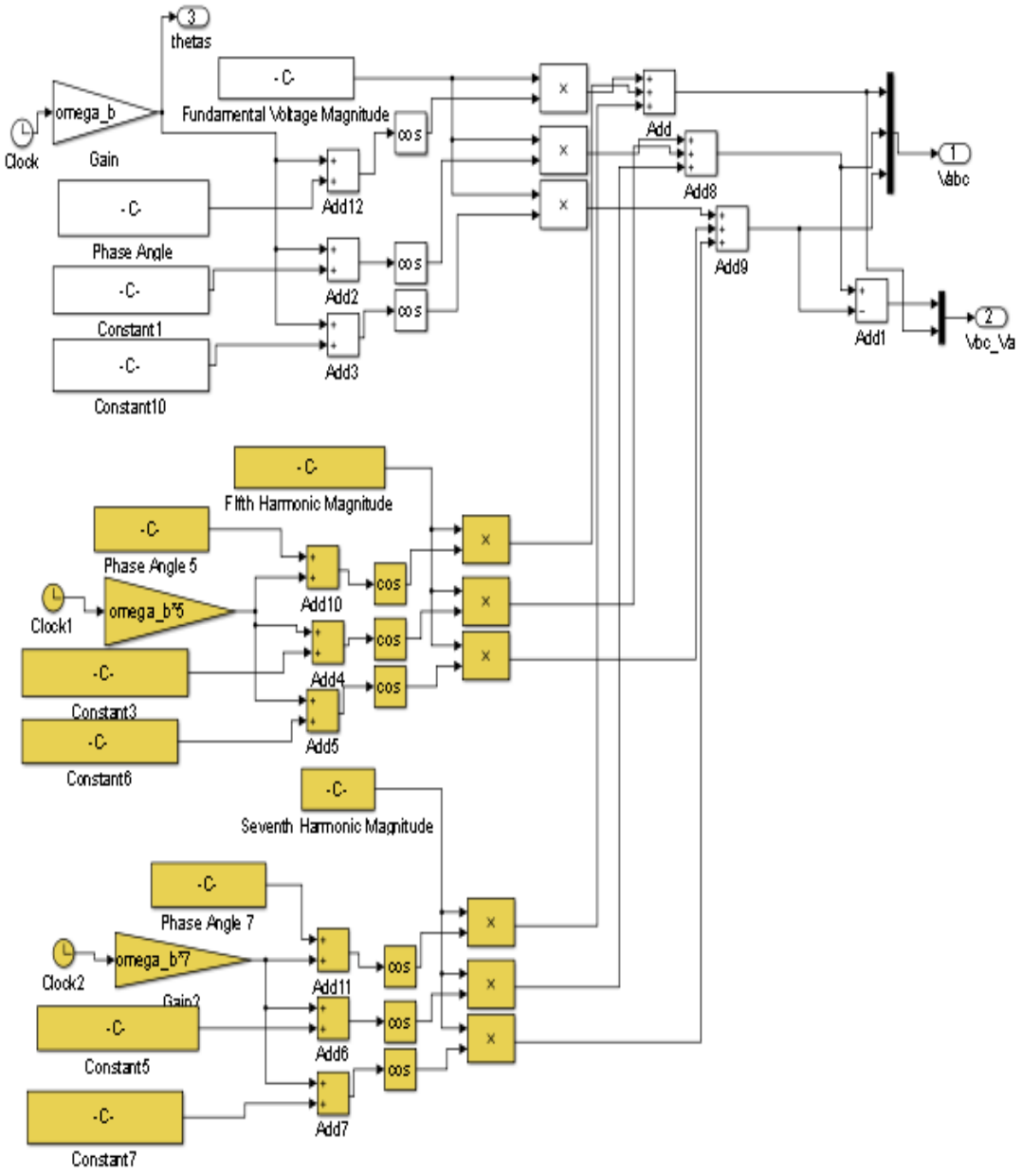

Figure 5. Simulink model of grid source voltage.

The simulated and measured stator harmonic currents agree within a twenty percent maximum error. This level of agreement is accepted as adequate for use in modeling a harmonic rejection controller. The measured and simulated V_{BC} and I_{as} are plotted together for both the sub-synchronous and super-synchronous data runs. The plots for the sub-synchronous data are shown in Figure 6.

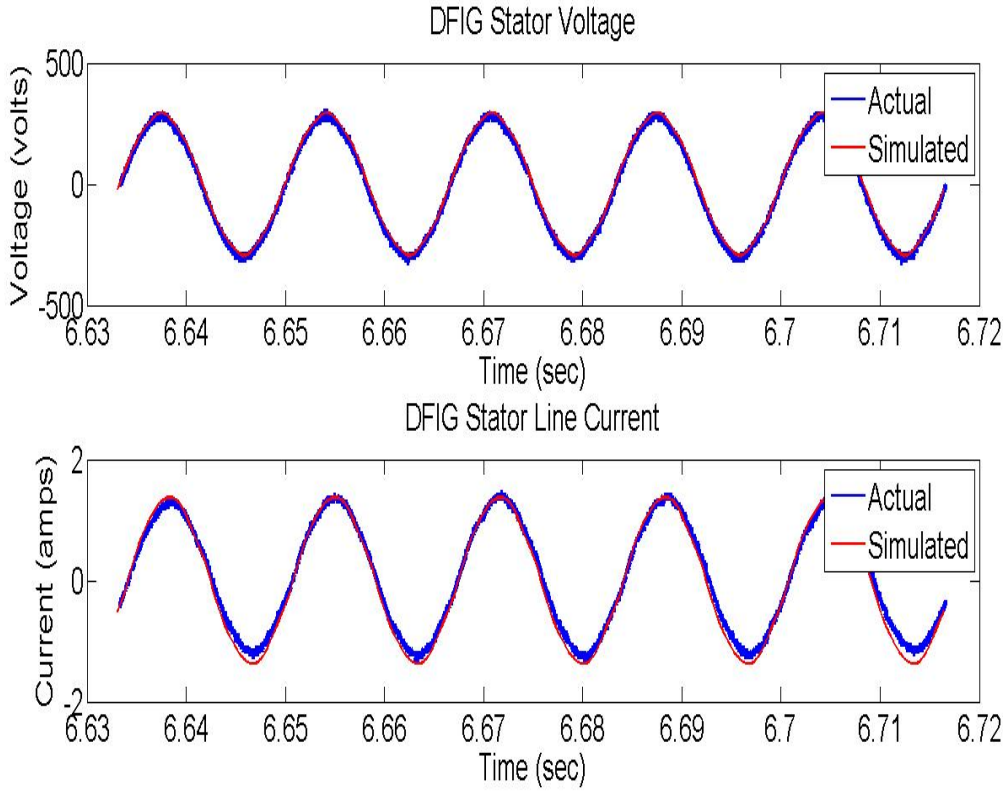

Figure 6. Measured and simulated stator voltage and current for the sub-synchronous data run.

The super-synchronous data is plotted in Figure 7.

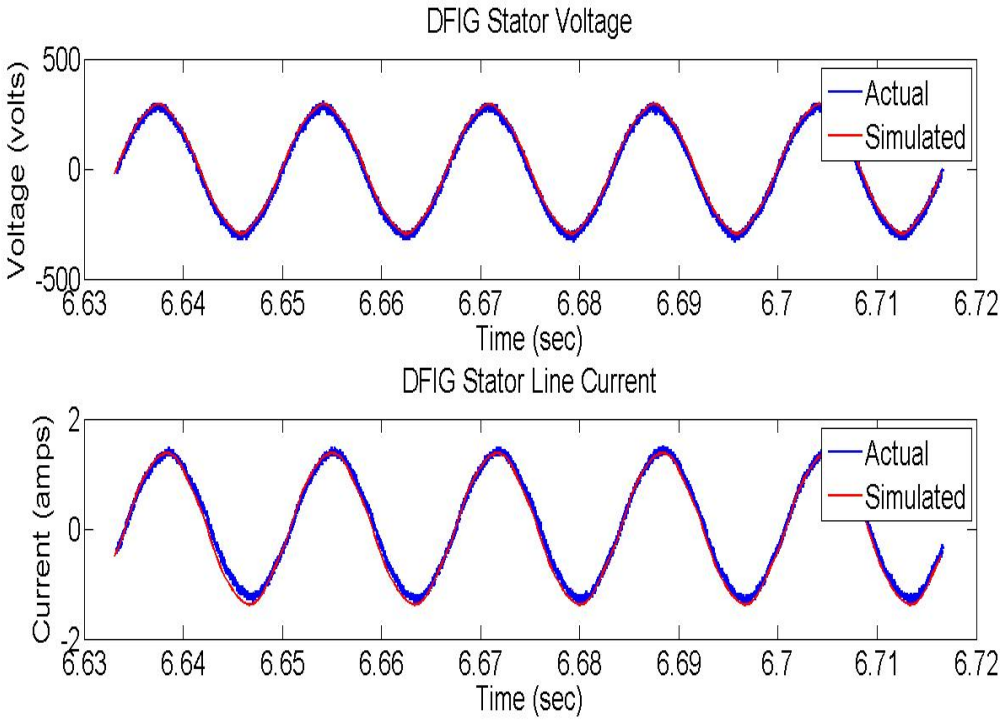

Figure 7. Measured and simulated stator voltage and current for the super-synchronous data run.

D. CHAPTER SUMMARY

The equations used to model the NPS DFIG system were presented in this chapter. The vector control strategy was explained and the Simulink model was presented. The effects of voltage harmonics on the stator current were compared with the Simulink model. The Simulink model was verified to be accurate and will be used to model the harmonic rejection controllers discussed in the next chapter.

IV. HARMONIC REJECTION TOPOLOGIES

Two harmonic rejection controller models were developed for this thesis. The theory behind each controller and results of applying the controller to the existing DFIG model [10] are presented in this chapter.

A. MRF CONTROLLER

1. Theory of Operation

The MRF controller is based upon a controller developed in [4]. The controller operates in the reference frame that rotates along with the harmonic that is being eliminated. Transforming the stator current into the frame of reference of the unwanted harmonic results in alternating current (AC) signals superimposed on a direct current (DC) signal. The DC signal corresponds to the harmonic, while the AC signals correspond to all of the other Fourier components of the electrical signal. A low pass filter extracts the DC component of the signal. The DC component (corresponding to the unwanted harmonic) is sent to a PI controller which has a commanded value set to zero. The output of the PI controller is transformed into the rotor reference frame and added to the existing v_{qr} and v_{dr} generated by the vector control portion of the rotor controller discussed in Chapter III. The block diagram for the MRF controller is shown in Figure 8.

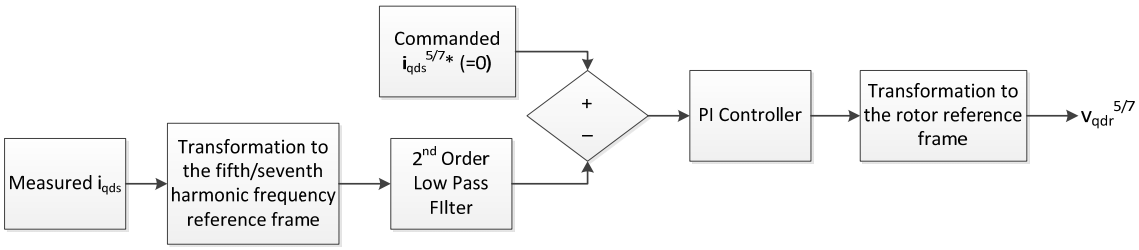

Figure 8. MRF controller block diagram.

There are a total of four different channels to the MRF controller: *q* and *d*-axis components for both the fifth and seventh harmonics present in the stator current. The Simulink block diagram for the rotor controller using the MRF rejection strategy is shown in Figure 9.

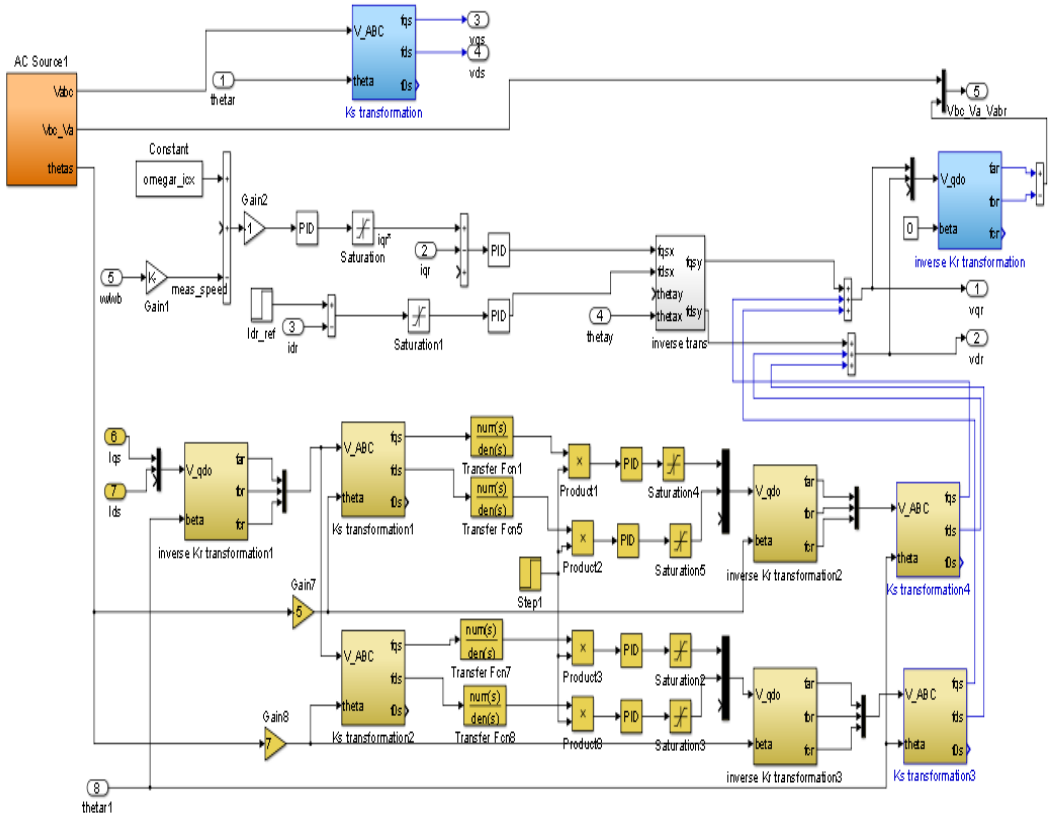

Figure 9. Simulink diagram of the MRF rotor controller.

The PI gains used in each of the channels of the MRF controller are shown in Table 4.

Table 4. PI gains for MRF controller.

	Value
Proportional Gain	100
Integral Gain	1000

The low-pass filter used was a second-order Butterworth filter with the transfer function [4]

$$G_{LPF} = \frac{\omega_c}{s^2 + \sqrt{2}s\omega_c + \omega_c^2} \tag{29}$$

where ω_c is the cutoff frequency for the filter. The value for ω_c used in the simulation was 20 radians/second.

2. Calculation of the Fundamental Reference Frame Angle

The fundamental reference frame angle θ_1 is used to transform the stator current into the fifth and seventh reference frame. The angle θ_1 corresponds to the angle of the maximum stator flux which is the basis for vector control. This angle is

$$\theta_1 = \theta_r + \theta_{slip}. \tag{30}$$

where θ_{slip} corresponds to the slip angle between the rotor and the stator flux corresponding to the fundamental component of the stator voltage. The method used for the NPS DFIG uses equation (28), which is distorted by the fifth and seventh voltage harmonics present in v_{qds}^s. The distorted θ_{slip} was originally used to transform between reference frames, which resulted in instability in the MRF controller. There are methods that can be implemented to accurately detect θ_1 [3], but for this thesis, θ_1 was taken directly from the source voltage information. This is an artificiality that can only be used because of the simulation; this distortion will have to be dealt with prior to actually implementing the controller.

3. MRF Controller Results

The controller was implemented and subjected to the conditions measured in both the super-synchronous and sub-synchronous data runs shown in Table 1. The resulting stator current harmonic content before and after controller activation is shown in Table 5.

Table 5. Stator current harmonic content before and after MRF controller activation.

	Sub-Synchronous Operation		Super-Synchronous Operation	
	Before Activation	After Activation	Before Activation	After Activation
Fifth Harmonic Stator Current (% of fundamental)	1.90	5.62×10^{-5}	1.95	7.02×10^{-5}
Seventh Harmonic Stator Current (% of fundamental)	0.83	1.75×10^{-5}	0.67	1.84×10^{-5}

The harmonic content in the stator current is effectively eliminated by the MRF controller. The pulsation in the electromagnetic torque caused by the harmonics was also simulated. The reduction in the torque pulsations for the sub-synchronous data run is shown in Figure 10.

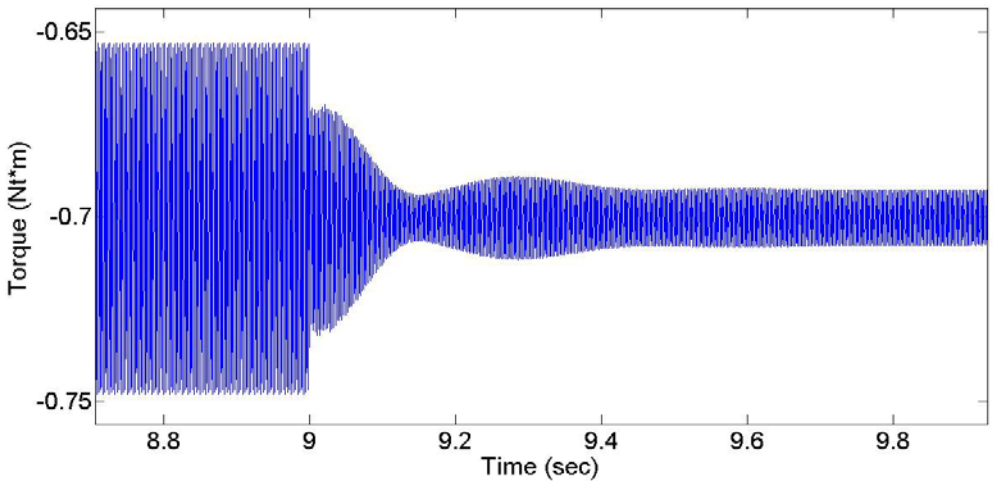

Figure 10. Effect of MRF controller on electromagnetic torque for the sub-synchronous data run.

The effect of the MRF controller on the torque for the super-synchronous data run is shown in Figure 11.

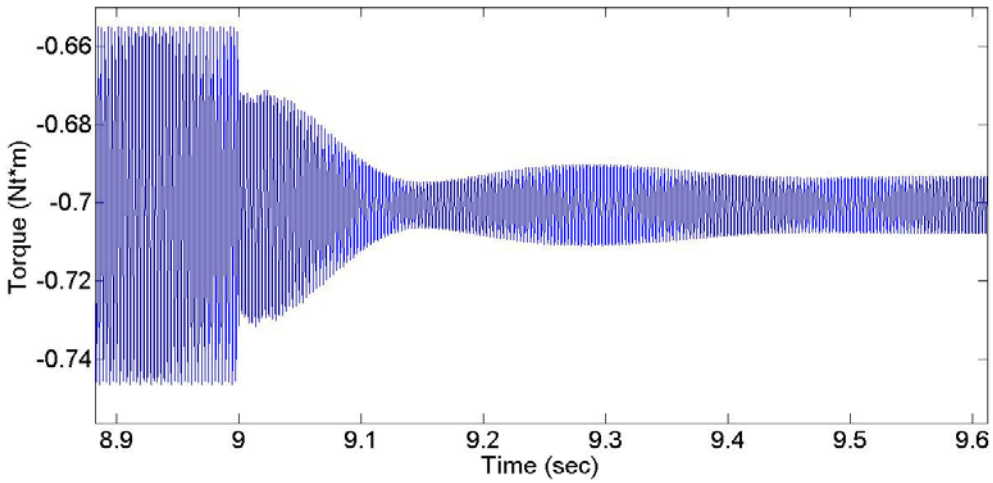

Figure 11. Effect of MRF controller on electromagnetic torque for the super-synchronous data run.

The MRF controller is enabled at nine seconds, and in both cases the steady-state torque pulsations were reduced to about twenty percent of their original value.

B. PR CONTROLLER

1. Theory of Operation

The PR controller is based upon a controller developed in [3]. The controller operates in the synchronous reference frame. In the synchronous reference frame, the fundamental stator current is a DC signal, the fifth harmonic is an AC signal with negative 360 Hz frequency (negative sequence harmonic), and the seventh harmonic is an AC signal with a positive 360 Hz frequency (positive sequence harmonic). The *q* and *d*-axis stator currents are transformed to the synchronous reference frame where they are applied to a filter with the transfer function [3]

$$G_R = \frac{2K_r\omega_c s}{s^2 + 2\omega_c s + (6\omega_b)^2} \tag{31}$$

where K_r is the resonant gain, and ω_c is equal to 20 radians/sec. The function G_R is a double integrator that is active at both the positive and negative 360 Hz. This allows for simultaneous filtering of both the fifth and seventh harmonics. The output from G_R is then added to the existing v_{qr} and v_{dr} generated by the vector control portion of the rotor

controller discussed in Chapter III. The block diagram for the PR controller is shown in Figure 12.

Figure 12. Block diagram for the PR controller.

The Simulink diagram for the PR rotor controller is shown in Figure 13.

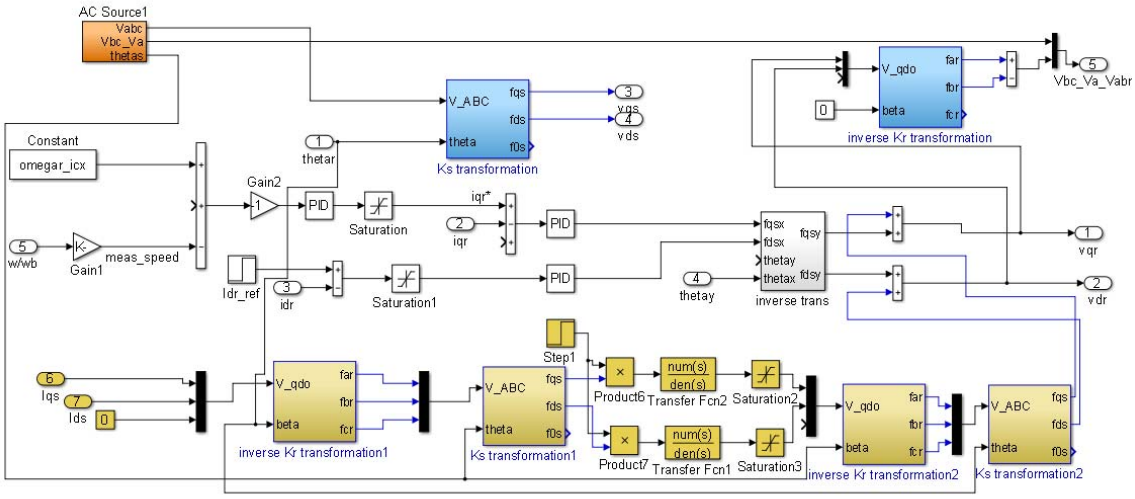

Figure 13. Simulink diagram of the PR rotor controller.

2. Calculation of the Fundamental Reference Frame Angle

The same instability seen in the MRF controller occurs in the PR controller if the harmonic distortion is not minimized in θ_1. The transformations used in this simulation also used the information from the source voltage generated in by Simulink. The same methods for avoiding the distortion in θ_1 referenced for the MRF controller apply to the PR controller.

3. PR Controller Results

The controller was implemented and subjected to the conditions measured in both the super-synchronous and sub-synchronous data runs shown in Table 1. The resulting stator current harmonic content before and after controller activation is shown in Table 6.

Table 6. Stator current harmonic content before and after PR controller activation.

	Sub-Synchronous Operation			Super-Synchronous Operation		
	Before Activation	After Activation		Before Activation	After Activation	
		K_r=1000	K_r=10000		K_r=1000	K_r=10000
Fifth Harmonic Stator Current (% of fundamental)	1.90	0.32	0.063	1.95	0.34	0.064
Seventh Harmonic Stator Current (% of fundamental)	0.83	0.14	0.031	0.67	0.12	0.026

The controller was simulated at $K_r = 1000$ and $K_r = 10000$ to illustrate the steady-state error's dependence on K_r. The results match the assertion made in [3] that the steady-state error varies approximately as the inverse of K_r. The reduction in the electrical torque fluctuation for the sub-synchronous data run is shown in Figure 14.

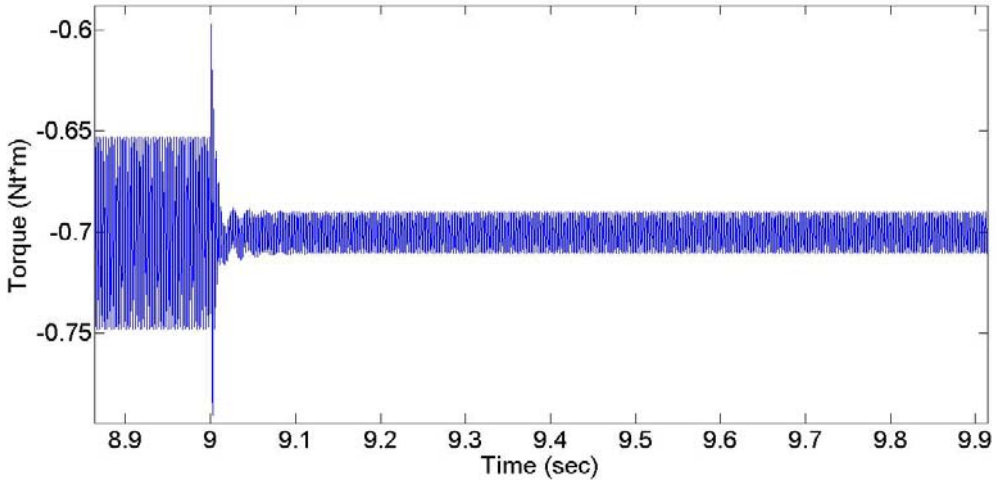

Figure 14. Effect of PR controller on electromagnetic torque for the sub-synchronous data run.

The reduction in the electrical torque fluctuation for the super-synchronous data run is shown in Figure 15.

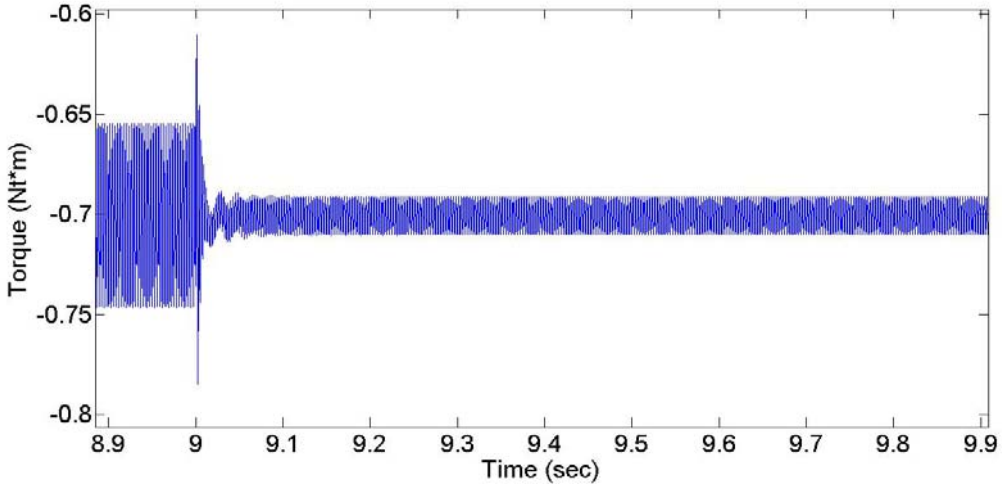

Figure 15. Effect of PR controller on electromagnetic torque for the super-synchronous data run.

The PR controller was enabled at nine seconds for both data runs and the torque fluctuations for both $K_r = 1000$ and $K_r = 10000$ were reduced to approximately twenty percent of their original value.

C. CHAPTER SUMMARY

The theory behind the PR and MRF harmonic rejection controllers was presented in this chapter. The simulated results of applying these controllers to a functional model of the DFIG used at NPS were also shown. Both controllers reduce the harmonic content of the stator current and reduce shaft torque fluctuations. The importance of properly calculating θ_1 was also discussed in relation to system stability.

THIS PAGE INTENTIONALLY LEFT BLANK

V. CONCLUSIONS AND RECOMMENDATIONS

A. COMPARING MRF AND PR CONTROLLERS

Both PR and MRF controllers would be viable options for reducing the harmonic content of the stator current for the DFIG. The advantages and disadvantages for each type of controller are summarized in Table 7.

Table 7. Advantages and disadvantages for the MRF and PR controllers.

Controller Type	Advantages	Disadvantages
PR	1. Fast response (<0.1 seconds to reach steady state once enabled) 2. Reduced torque fluctuations by 80% 3. Simultaneously filters both the fifth and seventh harmonics	1. Less reduction in stator current harmonics
MRF	1. Reduced torque fluctuations by 80% 2. Significantly reduced stator current harmonics	1. Slower response (approximately 0.5 seconds to reach steady state once enabled) 2. A controller is required for each harmonic

Both controllers reduced the harmonic content of the stator current and the torque fluctuations. The stator current harmonic reduction for each controller was adequate to reduce the torque fluctuations to approximately the minimum value possible. The remaining torque fluctuations were caused by the fluctuation in the stator flux, which was the result of the grid voltage harmonics. A stable DFIG wind system would be a great way to help the Department of Defense reach the goal of 25 percent renewable energy by 2025.

B. FUTURE RESEARCH

The PR and MRF controllers are ready for laboratory implementation. The calculation of a proper synchronous angle (to not include harmonic distortion) is required

for the controllers to function properly. Future research is required to implement a method to calculate this angle without distortion.

A linearized model of the DFIG used at NPS would aid in tuning the controllers for optimum performance. Proper tuning could distinguish which controller (PR or MRF) has better performance prior to implementing one of them.

APPENDIX. FILES AND DIAGRAMS

A. SIMULINK MODEL INITIAL CONDITIONS FILE

```
omega_b = 2*pi*60;
% omega2=-omega_b*1/14;

twopiby3 = 2*pi/3;
poles = 4;
polesby2J = poles/2/(2.04e-3*2);    %Inertia from Nytko thesis doubled
because DC machine is connected by a belt
Kpgain_speed=.033*2;
Kigain_speed=.0033*4;
Kpgain=15/2*10;    % Divide by 2 because Vdc=60 is half of 120 in the
FPGA program
Kigain=2/2*40;
%Parameters from Edwards thesis work for DFIG
rs=12;
rr = 4;
Xls =9/2;
Xm =180*0.6;    % no load
Xm =180*0.7;    % with generation
Xlr = (9+omega_b*400e-6)/2;

rsbyXls = rs/Xls;
rrbyXlr = rr/Xlr;
Xaq = 1/(1/Xm+1/Xls+1/Xlr);
Xad = Xaq;
XaqbyXls = Xaq/Xls;
XaqbyXlr = Xaq/Xlr;
XadbyXls = Xad/Xls;
XadbyXlr = Xad/Xlr;
V_phase = 220*sqrt(2)/sqrt(3);  %Peak value used in Simulink for source
model

% omegar_ic = omega_b*13/14;
psi_qsic=0;
psi_dsic=0;
psi_qric=0;
psi_dric=0;

%cutoff frequency for the resonant controller = 20 rad/sec from
%fifth/seventh paper
%omega_c = 2*pi*60;
omega_c= 20;
omega_c_theta_y= 2*2*pi*60;
Kr = 1000;
%lp pi controller gain
kp_lp = 100;
ki_lp = 1000;
```

B. SCRIPT FILE THAT CALLS THE DFIG SIMULINK MODEL

```
% Alex Julian, Giovanna Oriti, 25 May 12
% Modified by Seth Pierce, 01 May 13
clear all;
close all;

select_data_run_type=1;         %=1 for super-synchronous, =0 for sub-
synchronous

omega_b = 2*pi*60;

if (select_data_run_type==1)
    omegar_icx = 1.10*omega_b;
    volt_fund_mean_magn=  1.439503788846466e+02;
    volt_fund_mean_phase=-89.087746465851350;
    volt_fifth_mean_magn=2.090837759817524;
    volt_fifth_mean_phase=-1.013347590803720e+02;
    volt_seventh_mean_magn=0.868010167917528;
    volt_seventh_mean_phase=62.028270372187910;

else
    omegar_icx = omega_b*.7976;
    volt_fund_mean_magn=  1.439771855935957e+02;
    volt_fund_mean_phase=-89.273590872086900;
    volt_fifth_mean_magn=2.321642655421061;
    volt_fifth_mean_phase=-92.051349124310110;
    volt_seventh_mean_magn=0.877413077726262;
    volt_seventh_mean_phase=57.269559535853410;

end

%input_voltage_current_spectrum_V3   %remember to change this file to
fast or slow
%Vout_plot
%-------------------------------------------------------------------------
---------------------

% ------------------------------------------------------------------------
--------------------

t_on_controller = 9; % This is when the harmonic controller turns on

tstep=1/4200;
tstop=25;   % The dft's are both computed over a 2 sec interval, so
keep that in
            %  mind when choosing t_on_controller and tstop
%--------------

%sim DFIG_Thesisx;                  %uses pi control
sim DFIG_Thesis_with_six_harm_filter;       %uses high q method
```

```
figure(1);
plot(speed_sim(:,1),speed_sim(:,2),'b','linewidth',2)
title('Simulated speed');
legend('RPM','location','east');
grid;

%-------------------------------------------------------------------------
%This is the dft during a 2 sec period of ias after resonant controller

%-------------------------------------------------------------------------
-
%Trying to DFT the first period of the Vbc in this section and plot it

T = tstep;                      % Sample time
Fs = 1/T;
L = 1/60/tstep;                      % Length of signal
fo=Fs/(L);
t = (0:L-1)*T;                % Time vector

X(1:L)=0;
for q=0:L-1
    for l=0:L-1
        X(q+1)=speed_sim(l+1+500*L,3)*exp(-i*2*pi*q*l/(L))+X(q+1);
    end
end

cq_v=1/L*X;
cq_magn_v=abs(cq_v);
cq_phase_v=angle(transpose(cq_v))*180/pi;

% V_bc_DFT_magn=[volt_fund_mean_magn  volt_fifth_mean_magn
volt_seventh_mean_magn];
% V_bc_DFT_phase=[volt_fund_mean_phase volt_fifth_mean_phase
volt_seventh_mean_phase];
% I_as_DFT_magn=[curr_fund_mean_magn curr_fifth_mean_magn
curr_seventh_mean_magn];
% I_as_DFT_phase=[curr_fund_mean_phase curr_fifth_mean_phase
curr_seventh_mean_phase];
% plot_harm_freq=[60 300 420];
%
% figure(2)
% subplot(2,1,1)
% semilogx((1)*fo, 20*log10(cq_magn_v(2)/cq_magn_v(2)),'ro', (5)*fo,
20*log10(cq_magn_v(6)/cq_magn_v(2)),'ro',(7)*fo,
20*log10(cq_magn_v(8)/cq_magn_v(2)),'ro',
plot_harm_freq,20*log10(V_bc_DFT_magn/volt_fund_mean_magn),'b+','linewi
dth',4, 'MarkerSize',10)
% title('Magnitude Spectrum of Input Voltage')
% xlabel('Frequency (Hz)')
% ylabel('Magnitude (V)')
% axis([50 500 -50 0])
% grid on
%
```

```
% subplot(2,1,2)
% semilogx((0:8)*fo, cq_phase_v(1:9),'o',
plot_harm_freq,V_bc_DFT_phase,'+','linewidth',4, 'MarkerSize',10)
% title('Phase Spectrum of Input Voltage')
% xlabel('Frequency (Hz)')
% ylabel('Phase (Degrees)')
% axis([50 500 -180 180])
% grid on

X(1:L)=0;
for q=0:L-1
    for l=0:L-1
        X(q+1)=speed_sim(l+1+500*L,6)*exp(-i*2*pi*q*l/(L))+X(q+1);
    end
end

cq_v=1/L*X;
cq_magn_v=abs(cq_v);
cq_phase_v=angle(transpose(cq_v))*180/pi;

figure(3)
subplot(2,1,1)
stem((0:8)*fo, 2*cq_magn_v(1:9))
title('Magnitude Spectrum of Phase A Input Voltage')
xlabel('Frequency (Hz)')
ylabel('Magnitude (V)')

subplot(2,1,2)
stem((0:8)*fo, cq_phase_v(1:9))
title('Phase Spectrum of Phase A Input Voltage')
xlabel('Frequency (Hz)')
ylabel('Phase (Degrees)')
%-------------------------------------------------------------------------
--

%-------------------------------------------------------------------------
-
%Trying to DFT the steady state stator current prior to control

% T = tstep;                      % Sample time
% Fs = 1/T;
% L = 1/60/tstep;                      % Length of signal
% fo=Fs/(L);
% t = (0:L-1)*T;                % Time vector

% X(1:L)=0;
% for q=0:L-1
%     for l=0:L-1
%         X(q+1)=speed_sim(l+1+500*L,5)*exp(-i*2*pi*q*l/(L))+X(q+1);
%     end
% end
%
% cq_i=1/L*X;
% cq_magn_i=abs(cq_i);
```

```
% cq_phase_i=angle(transpose(cq_i))*180/pi;

cq_i(1:L)=0;
for q=0:L-1
%     XX=x((d*L+1):(d*L+1+L))*exp(-1i*2*pi*q*(0:L-1)/(L));
    cq_i(q+1)=dot(speed_sim((500*L+1):(500*L+L),5),exp(-1i*2*pi*q*(0:L-
1)/(L)))/L;
end

cq_magn_i=abs(cq_i);
cq_phase_i=angle(transpose(cq_i))*180/pi;

figure(4)
subplot(2,1,1)
stem((0:8)*fo, 2*cq_magn_i(1:9))
title('Magnitude Spectrum of Stator Current Before Controller
Activation')
xlabel('Frequency (Hz)')
ylabel('Magnitude (Amps)')

subplot(2,1,2)
stem((0:8)*fo, cq_phase_i(1:9))
title('Phase Spectrum of Stator Current')
xlabel('Frequency (Hz)')
ylabel('Phase (Degrees)')
%-------------------------------------------------------------------------
--

%-------------------------------------------------------------------------
-
%Trying to DFT the steady state stator current after controller turns
on

% T = tstep;                      % Sample time
% Fs = 1/T;
% L = 1/60/tstep;                      % Length of signal
% fo=Fs/(L);
% t = (0:L-1)*T;                % Time vector

X(1:L)=0;
for q=0:L-1
    for l=0:L-1
        X(q+1)=speed_sim(l+1+1450*L,5)*exp(-i*2*pi*q*l/(L))+X(q+1);
    end
end

cq_i=1/L*X;
cq_magn_i=abs(cq_i);
cq_phase_i=angle(transpose(cq_i))*180/pi;

figure(5)
subplot(2,1,1)
stem((0:8)*fo, 2*cq_magn_i(1:9))
```

```
title('Magnitude Spectrum of Stator Current After Controller
Activated')
xlabel('Frequency (Hz)')
ylabel('Magnitude (Amps)')

subplot(2,1,2)
stem((0:8)*fo, cq_phase_i(1:9))
title('Phase Spectrum of Stator Current')
xlabel('Frequency (Hz)')
ylabel('Phase (Degrees)')
%-------------------------------------------------------------------------
--



% figure(6)
% axes('FontSize',22)
% subplot(2,1,1)
%
plot(time_vec(1:41660)+6.7333,data_vec_v(1:41660),speed_sim(27860:27860
+5*L,1),speed_sim(27860:27860+5*L,3),'r','linewidth',2)
% title('Line-Line Stator Voltage (Vbc)')
% xlabel('Time (sec)')
% ylabel('Voltage (volts)')
% legend('Actual','Simulated')
%
% subplot(2,1,2)
% plot(time_vec(1:41660)+6.7333,data_vec_i(1:41660),
speed_sim(27860:27860+5*L,1),speed_sim(27860:27860+5*L,5),'r','linewidt
h',2)
% title('Stator Line Current (Ias)')
% xlabel('Time (sec)')
% ylabel('Current (amps)')
% legend('Actual','Simulated')

figure(7)
plot(speed_sim(:,1), speed_sim(:,7))
%title('Electromagnetic Torque')
xlabel('Time (sec)')
ylabel('Torque (Nt*m)')
```

C. CALCULATION OF STATOR CURRENT AND GRID VOLTAGE HARMONICS

```
if (select_data_run_type==1)
    data_v=xlsread('Tek_CH1_Wfm_1990_Vbc.csv');
    data_i=xlsread('Tek_CH2_Wfm_1990_Ias.csv');
else
    data_v=xlsread('Tek_CH1_Wfm_1435_Vbc.csv');
    data_i=xlsread('Tek_CH2_Wfm_1435_Ias.csv');
end

len = length(data_i);
data=data_i(15:len,1:2);
datav=data_v(15:len,1:2);
```

```
newlen=length(data); %this equals 10,000 rows col_1-time col_2-vout
time_vec=data(:,1);  %column 1 only from xls - time
data_vec_i=data(:,2);  %column 2 only from xls - vout
data_vec_v=datav(:,2);  %column 2 only from xls - vout

Fs=500e3; %sampling frequency from oscope
len2=len-15; %obtains number of samples in one cycle
k=0:len2-1;       %create a vector from 0 to newlen-1
T=len2/Fs;        %get the frequency interval
freq=k/T;         %create the frequency range




figure(1);
axes('FontSize',22)
% plot(time_vec(1:len2),data_vec_i(1:len2));
% hold on;
plot(time_vec(1:len2)+0.1,data_vec_v(1:len2));
v1period=data_vec_v(1:len2);
title('DFIG Source Line Voltage (B-C)');
xlabel('Time'); ylabel('Volts');
grid on
hold off;
% legend('I_a_s','V_b_c/20','Location','Northeast');

Ts=time_vec(50)-time_vec(49);
fs=1/Ts;
L=8332;
fo=fs/L;
k = 0;              %This index allows us to move a window along the
sine wave for 10 cycles
k2 = 0;
x(1:len2)=data_vec_v(1:len2);
x2(1:len2)=data_vec_i(1:len2);
for d=0:11


cq(1:L)=0;
for q=0:L-1
%     XX=x((d*L+1):(d*L+1+L))*exp(-1i*2*pi*q*(0:L-1)/(L));
    cq(q+1)=dot(x((d*L+1):(d*L+L)),exp(-1i*2*pi*q*(0:L-1)/(L)))/L;
end

cq_magn_v=abs(cq);
cq_phase_v=angle(transpose(cq))*180/pi;

if (d==0)
    figure(2);
    axes('FontSize',22)
    stem((0:8)*fo, (cq_magn_v(1:9)/cq_magn_v(2)))
    set(gca,'yscal','log')
```

```
end

volt_fund_magn(d+1)=cq_magn_v(2);
volt_fifth_harm_magn(d+1)=cq_magn_v(6);
volt_seventh_harm_magn(d+1)=cq_magn_v(8);
volt_fund_phase(d+1)=cq_phase_v(2);
volt_fifth_harm_phase(d+1)=cq_phase_v(6);
volt_seventh_harm_phase(d+1)=cq_phase_v(8);

cq_i(1:L)=0;
for q=0:L-1
%     XX=x((d*L+1):(d*L+1+L))*exp(-1i*2*pi*q*(0:L-1)/(L));
    cq_i(q+1)=dot(x2((d*L+1):(d*L+L)),exp(-1i*2*pi*q*(0:L-1)/(L)))/L;
end



cq_magn_i=abs(cq_i);
cq_phase_i=angle(transpose(cq_i))*180/pi;

curr_fund_magn(d+1)=cq_magn_i(2);
curr_fifth_harm_magn(d+1)=cq_magn_i(6);
curr_seventh_harm_magn(d+1)=cq_magn_i(8);
curr_fund_phase(d+1)=cq_phase_i(2);
curr_fifth_harm_phase(d+1)=cq_phase_i(6);
curr_seventh_harm_phase(d+1)=cq_phase_i(8);
end

volt_fund_mean_magn=mean(volt_fund_magn);
volt_fund_mean_phase=mean(volt_fund_phase);
volt_fifth_mean_magn=mean(volt_fifth_harm_magn);
volt_fifth_mean_phase=mean(volt_fifth_harm_phase);
volt_seventh_mean_magn=mean(volt_seventh_harm_magn);
volt_seventh_mean_phase=mean(volt_seventh_harm_phase);

v_fifth_perc=volt_fifth_mean_magn/volt_fund_mean_magn;
v_sev_perc=volt_seventh_mean_magn/volt_fund_mean_magn;


curr_fund_mean_magn=mean(curr_fund_magn);
curr_fund_mean_phase=mean(curr_fund_phase);
curr_fifth_mean_magn=mean(curr_fifth_harm_magn);
curr_fifth_mean_phase=mean(curr_fifth_harm_phase);
curr_seventh_mean_magn=mean(curr_seventh_harm_magn);
curr_seventh_mean_phase=mean(curr_seventh_harm_phase);
```

D. SIMULINK MODEL DIAGRAMS

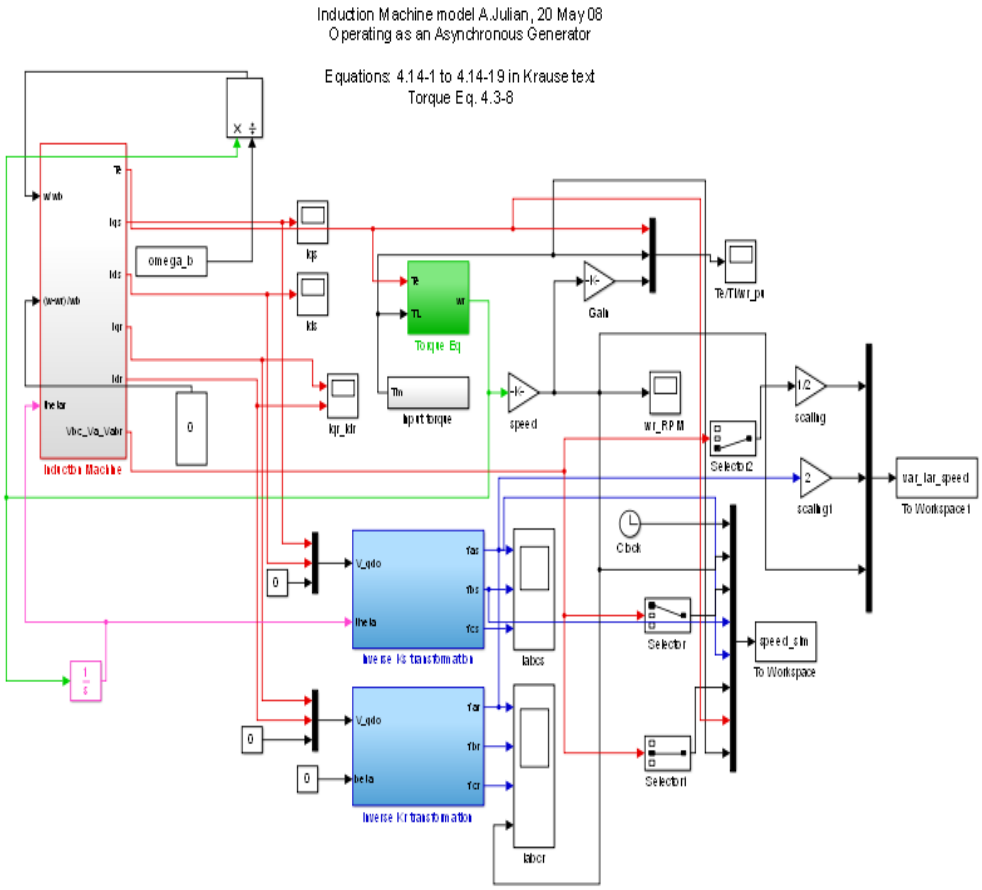

Figure 16. Top-level DFIG model diagram.

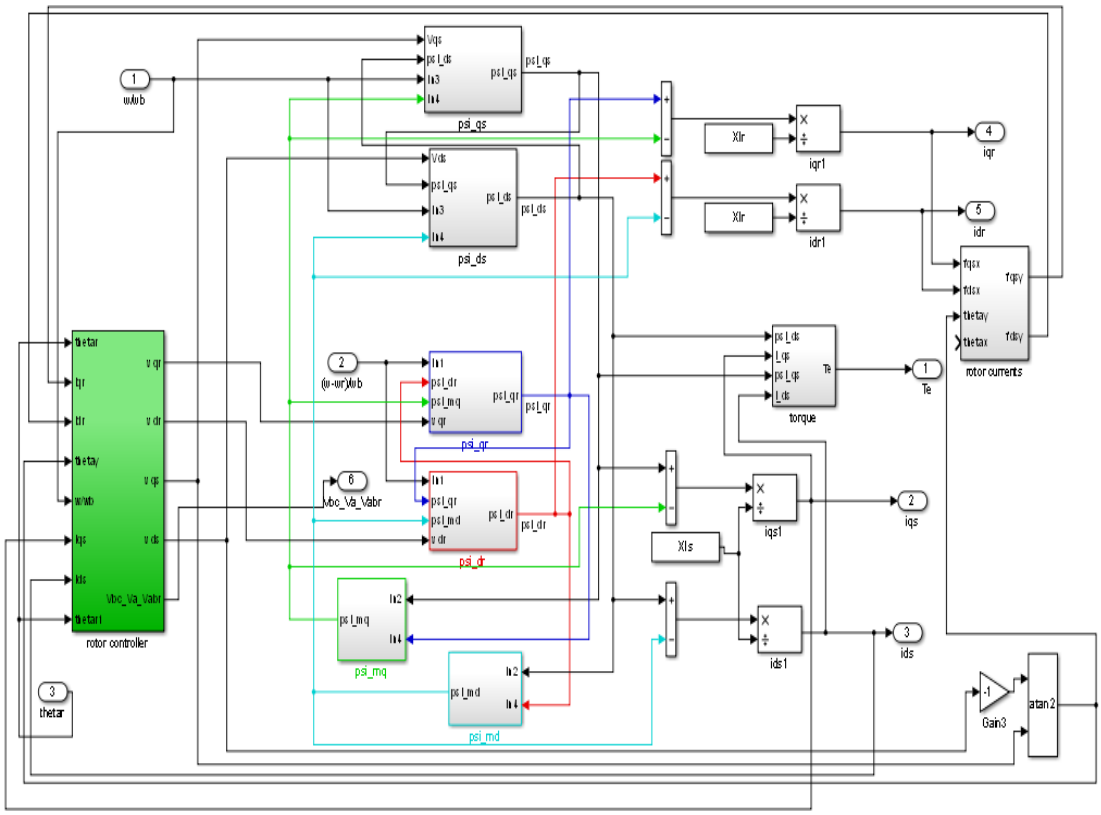

Figure 17. Simulink model diagram of the induction machine.

LIST OF REFERENCES

[1] John Warner National Defense Authorization Act for Fiscal Year 2007, Public Law no. 109-364, section 2852, 2006.

[2] R. Pena et al., "Doubly fed induction generator using back-to-back PWM converters and its application to variable-speed wind-energy generation," *IEEE Proc. Electr. Power Appl.*, vol. 143, no. 3, pp. 231–241, May 1996.

[3] L. Changjin et al., "Stator current harmonic control with resonant controller for doubly fed induction generator," *IEEE Trans. on Power Electronics*, vol. 27, no.7, pp. 3207–3220, July 2012.

[4] C. Wenjie et al.,"Stator harmonic current suppression for DFIG wind power system under distorted grid voltage," *3rd IEEE International Symposium on Power Electronics for Distributed Generation Systems*, Aalborg, Denmark, pp. 307–314, 2012.

[5] G. W. Edwards, "Wind power generation emulation via doubly-fed induction generator control," M.S. thesis, Naval Postgraduate School, Monterey, CA, 2009.

[6] J. R. Derges, "Torque control of a separate-winding excitation DC motor for a dynamometer," M.S. thesis, Naval Postgraduate School, 2010.

[7] *IEEE Recommended Practices and Requirements for Harmonic Control in Electrical Power Systems*, IEEE Standard 519, 1993.

[8] A. V. Oppenheim, A. S. Willsky, S. H. Nawab, *Signals and Systems*, Upper Saddle River, NJ: Prentice Hall, 2nd ed., 1997.

[9] P.C. Krause, O. Wasynczjk, S. D. Sudhoff, *Analysis of Electric Machinery and Drive Systems*, Hoboken NJ: John Wiley & Sons, 2002.

[10] A. L. Julian, "Induction machine model operating as an asynchronous generator," class notes for EC4130 (Advanced Electrical machinery Systems), Naval Postgraduate School, Monterey, CA, summer 2012.

THIS PAGE INTENTIONALLY LEFT BLANK

INITIAL DISTRIBUTION LIST

1. Defense Technical Information Center
   Ft. Belvoir, Virginia

2. Dudley Knox Library
   Naval Postgraduate School
   Monterey, California